Multiparametric MRI for evaluation of tumour treatment response

Studies of ^{177}Lu-octreotate therapy of neuroendocrine tumour

Mikael Montelius

Department of Radiation Physics
Institute of Clinical Sciences
Sahlgrenska Cancer Center
Sahlgrenska Academy at University of Gothenburg

UNIVERSITY OF GOTHENBURG

Gothenburg 2016

Cover illustration by Mikael Montelius

Multiparametric MRI for evaluation of tumour treatment response
Studies of ^{177}Lu-octreotate therapy of neuroendocrine tumour

mikael.montelius@radfys.gu.se

ISBN 978-91-628-9963-9 (Print)
ISBN 978-91-628-9964-6 (PDF)
http://hdl.handle.net/2077/44927

Printed by Ineko
Gothenburg, Sweden 2016

“Feel the fear and do it anyway”

Susan Jeffers

Abstract

Multiparametric MRI for evaluation of tumour treatment response

Studies of ^{177}Lu-octreotate therapy of neuroendocrine tumour

Mikael Montelius
Department of Radiation Physics, Institute of Clinical Sciences,
Sahlgrenska Academy at University of Gothenburg, Sweden, 2016

Clinical assessment of tumour response to treatment largely relies on estimates of tumour size by, *e.g.*, measuring the largest tumour diameters on magnetic resonance (MR) or computed tomography (CT) images, weeks or months after treatment. However, most tumours are heterogeneous, and treatment may result in different effects in different parts of the tumour. Therefore, non-invasive methods sensitive to biological effects that precede changes in tumour size would improve our understanding of tumour biology and therapeutic effects, facilitate personalized treatments and speed up development of anti-cancer therapeutics. MR methods have the potential to provide non-invasive imaging biomarkers of the relevant tumour biology, but the understanding of the information provided by MR methods is still limited.

The aim of this project to was to improve the understanding and evaluate the feasibility of multiparametric MR methods for therapy response assessment of tumours after radionuclide therapy.

Mice xenografted with human neuroendocrine tumours received 15 MBq ^{177}Lu-octreotate i.v. on day 0, and MR imaging experiments were performed on days -1, 1, 3, 8 and 13, using dynamic contrast enhanced-, quantitative T1 and T2*- and diffusion weighted MR on a 7T small animal MR system. Optimization studies were performed to improve tissue model parameter estimates, and to ensure accurate MR based tumour volume estimation for response verification. MR parameter maps were spatially registered to corresponding histologically stained tumour section for correlation analysis, and tumour tissue samples were analysed using quantitative proteomics.

Several statistically significant correlations were found between MR parameters and histological tumour characteristics, as well as with proteins associated with radiobiological effects on tumours, and collectively evaluated they provided information on apoptotic and proliferative activity, microvascular density and fibrosis in tumours, which are all important prognostic tumour characteristics. Spatial and temporal MR parameter variations before and after therapy seem to be predictive of tumour shrinkage or stabilization. Most effects on MR parameters were seen already one day after treatment initiation.

This work demonstrates the feasibility of multiparametric MR for therapy response assessment in an animal tumour model, and highlights the importance of spatial and temporal evaluation of the MR parameters. Future efforts should include improvement of methods for spatial registration of in vivo MR images and ex vivo histological sections. For clinical applications, MR acquisition times need to be reduced.

Keywords: Cancer, Functional imaging, IVIM, MRI, DWI, DCE, histology, ^{177}Lu-octreotate, small intestine neuroendocrine tumour, NET, diffusion, perfusion, semi-quantitative, proteomics, ionizing radiation, biology, imaging biomarker

ISBN: 978-91-628-9963-9
E-publication: http://hdl.handle.net/2077/44927

Populärvetenskaplig sammanfattning

Idag vet man att tumörer oftast är heterogena, vilket innebär att vissa områden i tumören kan svara bra på behandling, medan andra svarar sämre. Detta kan till exempel bero på varierande genomblödning (perfusion), vilket kan hindra transport av läkemedel till tumörvävnaden, eller syrebrist, vilket försämrar effekten av strålning. Man kan därför inte se tumören som en enkel, homogen massa av tumörceller, men de metoder som är kliniskt tillgängliga idag för att säkerställa att tumören svarar på behandling bygger på ett sådant koncept. Storleken på tumören skattas genom att man mäter dess diametrar t.ex. på magnetresonans (MR)- eller datortomografi (DT)-bilder, och man måste vänta länge mellan mätningarna för att säkerställa svar, eftersom metoden har låg noggrannhet och känslighet för små förändringar i tumörvolym. Det innebär stora risker för patienten, eftersom ineffektiv behandling upptäcks i ett sent skede, vilket kan innebära sämre chanser till bot. Om det istället fanns metoder för att mäta de biologiska effekterna på tumören som sker före tumörvolymen påverkas, skulle man tidigare upptäcka ineffektiv behandling, bespara patienten onödigt lidande och kraftigt minska kostnaderna för samhället. Heterogeniteten kräver dock att metoderna visar hur alla delar av tumören svarar, och man behöver kunna studera utvecklingen i tumören före, under och efter behandlingen, vilket kräver att metoderna är icke-invasiva. När effekter av behandling studeras bör bildgivande metoder i sig inte ge någon stråldos till tumören, eftersom det kan påverka effekterna som studeras. Om vi hade tillgång till sådana metoder skulle vår kunskap om tumörbiologin och behandlingseffekter öka, och det skulle innebära snabbare framställning och test av nya cancerläkemedel.

MR-tekniker är icke-invasiva, och de kan användas för att avbilda hela tumören med mycket god detaljupplösning och bildkontrast. De har dessutom visat stor potential för mätning av relevanta biologiska effekter efter tumörbehandling, men förståelsen av kopplingen mellan de vävnadsparametrar man kan härleda från olika MR-tekniker och den underliggande tumörbiologin är begränsad. Syftet med detta avhandlingsprojekt var därför att öka förståelsen av den information som erhålls från olika MR-avbildningar av tumören, och därmed öka möjligheterna att använda dessa metoder för att mäta tumörsvar efter radionuklidterapi.

Som tumörmodell användes naken mus med human, neuroendokrin tunntarmstumör växande under huden. Tumörerna avbildades med flera olika MR-tekniker dagen före behandling (dag -1), i ett MR-system (7T) för smådjur. Dag 0 injicerades 15 MBq ^{177}Lu-octreotate i en svansven, och dag 1, 3, 8 och 13 upprepades MR-avbildningarna. Efter den sista avbildningen avlivades djuret, tumören delades parallellt med ett av de avbildade planen i tumören, och anatomiska riktningar färgkodades med vävnadsbläck i tumörkanterna. Dessa färgmarkeringar användes sedan för att matcha histologiskt infärgade och digitaliserade vävnadssnitt med MR-parameterbilder. Innan vävnadsparametrar beräknades från MR-bilderna, optimerades vissa modellanpassningsmetoder, bl.a. med hjälp av datorsimuleringar, för att säkerställa god kvalitet på parametrarna. En MR-avbildningsmetod optimerades för bestämning av tumörvolym med hög noggrannhet, vilket användes

för att verifiera tumörsvar. Vävnadsparameterkartor beräknades från MR-avbildningarna, och med hjälp av digital bildregistrering mot motsvarande histologiskt infärgat tumörsnitt undersöktes sambanden mellan MR-parametrar och tumörbiologi på pixelnivå. MR-parametrar jämfördes även mot proteinuttryck, som framställdes med kvantitativ proteomik på vävnadsprover.

Flera statistiskt signifikanta samband kunde påvisas mellan MR-parametrar och de biologiska egenskaper hos tumören som speglades i histologiparametrarna, men även mellan MR-parametrar och nivåer av proteinuttryck för proteiner som associerats med radiobiologiska effekter i tumörer. Den sammanlagda informationen som erhölls från MR-parametrarna kunde användas för att påvisa pågående apoptos (programmerad celldöd som t.ex. kan ske efter strålningsinducerad DNA-skada), proliferation (celldelning/tillväxt), mikrovaskulär densitet (förekomst av kärl/kapillärer vilket krävs för t.ex. syresättning) och fibros (vävnadsform som kan uppstå efter tidigare celldöd) vilka är kliniskt viktiga prognostiska tumörparametrar. Variationer av MR-parametrar inom tumören, och över tid efter behandling, kunde användas för att förutsäga vilka tumörer som skulle krympa och vilka som tillfälligt skulle stanna upp eller växa långsammare, och de flesta förändringarna i MR-parametrarna kunde ses redan dagen efter behandlingen. En viktig observation var att flera MR-parametrar som kunde användas för att skilja de olika svarande tumörgrupperna från varandra endast visade tillfälliga förändringar under uppföljningstiden, och att vissa parametrar endast kunde användas för att skilja grupperna om de analyserades lokalt i tumören, t.ex. i mer perifera delar, medan ett medelvärde av parametern över hela tumören inte förmådde skilja grupperna.

I detta arbete visas att det är möjligt att, genom att utläsa flera MR-parametrar från samma avbildningstillfälle, få ut viktig information om hur tumören svarar på behandling, och att det är viktigt att läsa ut informationen regionalt, och inte bara som ett medelvärde för hela tumören, samt att viktig information finns i hur parametrarna varierar efter behandlingen, såväl som i parametrarnas värden före behandling. För fortsatta studier inom detta område behövs bättre metoder för att säkerställa att MR-parametrar matchas bra mot vävnaden som analyseras efter att tumören avlägsnats. Innan metoderna kan användas kliniskt måste dessutom avbildningsteknikerna bli snabbare, och de biologiska kopplingarna som visas i detta arbete måste verifieras i flera studier på djur, samt i patienter.

List of papers

This doctoral thesis is based on the following four papers, which will be referred to in the text by Roman numerals:

I. **Mikael Montelius**, Maria Ljungberg, Michael Horn, Eva Forssell-Aronsson, *Tumour size measurement in a mouse model using high resolution MRI*. BMC Medical Imaging, 2012 **12**:12

II. Oscar Gustafsson, **Mikael Montelius**, Göran Starck, Maria Ljungberg, *Impact of prior distributions and central tendency measures on Bayesian intravoxel incoherent motion model fitting* (Manuscript)

III. **Mikael Montelius**, Oscar Gustafsson, Johan Spetz, Ola Nilsson, Eva Forssell-Aronsson, Maria Ljungberg, *Multiparametric MR evaluation of small intestine neuroendocrine tumour tissue characteristics correlated to histological analyses* (Manuscript)

IV. **Mikael Montelius**, Johan Spetz, Oscar Gustafsson, Evelin Berger, Ola Nilsson, Maria Ljungberg, Eva Forssell-Aronsson, *Identification of potential MR derived biomarkers for tumour response to ^{177}Lu-octreotate therapy in an animal model of small intestine neuroendocrine tumour* (Manuscript)

Related presentations

Montelius M., Spetz J., Gustafsson O., Ljungberg M., Forssell-Aronsson E. *Multiparametric MRI (mpMRI) for spatiotemporal characterization of tumor tissue response to radionuclide treatment.* Poster at the Radiation research society (RRS) 62nd annual meeting, October 16-19, 2016, Waikoloa Village, HI, USA

Spetz J., **Montelius M.**, Ljungberg M., Helou K., Forssell-Aronsson E. *Spatial proteomic analysis of GOT1 human small intestine neuroendocrine tumor in nude mice following ^{177}Lu-octreotate therapy* Poster at the Radiation research society (RRS) 62nd annual meeting, October 16-19, 2016, Waikoloa Village, HI, USA

Gustafsson O., **Montelius M.**, Starck G., Ljungberg M. *An assessment of Bayesian IVIM model fitting.* Poster at the International Society for Magnetic Resonance in Medicine (ISMRM), May 7-13, 2016, Singapore

Montelius M., Gustafsson O., Andersson M., Forssell-Aronsson E., Hultborn R., Ottosson S., Carlsson G., Lange S., Ljungberg M. *IVIM reveals increased blood perfusion of liver metastases after oral intake of Salovum®* Oral presentation at the European Society for Magnetic Resonance in Medicine and Biology (ESMRMB), 2015, Edinburgh, Scotland, UK

Montelius M., Ljungberg M., Forssell-Aronsson E. *Radiation induced effects on the solid GOT1 tumor model measured non-invasively using diffusion weighted magnetic resonance imaging.* Oral presentation at the Swedish Cancer Society organization group for oncological radionuclide therapy winter meeting, 2015, Umeå, Sweden

Montelius M., Ljungberg M., Forssell-Aronsson E. *Non-invasive, in-vivo assessment of radiation induced effects on solid GOT1 tumors using diffusion weighted magnetic resonance imaging.* Poster at RRS-2014 conference, Las Vegas, Nevada, USA

Montelius M., Ljungberg M., Forssell-Aronsson E. *Diffusion weighted MRI for non-invasive in-vivo assessment of radionuclide treatment effects on solid GOT1 tumors.* Poster at EANM-2014 conference, Gothenburg, Sweden

Montelius M., Ljungberg M., Forssell-Aronsson E. *Optimal ROI Size for Parameter Determination in IVIM Imaging.* Poster at EANM-2012 conference, Milano, Italy

Montelius M., Ljungberg M., Forssell-Aronsson E. *Optimal ROI Size for IVIM Imaging parameter determination.* Poster at ESMRMB-2012 conference, Lisbon, Portugal

Montelius M., Ljungberg M., Forssell-Aronsson E. *Determination of small tumor volumes in mice using MRI.* Poster at ESMRMB-2011 conference, Leipzig, Germany

Montelius M., Ljungberg M., Forssell-Aronsson E. *MATLAB tool for segmentation and re-creation of 1H-MRS volumes of interest in MRI image stacks.* Poster at ESMRMB-2009 conference, Antalya, Turkey

Table of Contents

Abbreviations

2/3D	2/3-dimensional
ADC	Apparent diffusion coefficient
AT	Arrival time
AUCn	Area under the curve (normalised)
BE	Brevity of enhancement
CER	Contrast enhancement ratio
CT	Computed tomography
D	Diffusion coefficient
*D**	Pseudo-diffusion coefficient
DCE	Dynamic contrast enhanced
DNA	Deoxyribonucleic acid
DOTA	Dodecanetetraacetic acid
DTPA	Diethylenetriaminepentaacetic acid
DWI	Diffusion weighted imaging
EES	Extracellular extravascular space
ex vivo	Out of the living
f	Perfusion fraction
FD	Fibrotic density
FDG-PET	Fluoro deoxyglucose positron emission tomography
^{18}F	Fluor-18
Gd	Gadolinium
GO	Gene ontology
Gy	Gray
HE	Haematoxylin
IFP	Interstitial fluid pressure
i.p.	Intraperitoneal
in vivo	Within the living
IS	Initial slope
IVIM	Intravoxel incoherent motion
i.v.	Intravenous
lasso	Least absolute shrinkage and selection operator
LC-MS	Liquid chromatography-mass spectrometry

^{177}Lu	Lutetium-177
MBq	Megabecquerel
MRI	Magnetic resonance imaging
MRS	Magnetic resonance spectroscopy
MT	Masson Trichrome
MVD	Micro-vessel density
NET	Neuroendocrine tumour
NS	Negative slope
^{15}O	Oxygen-15
PCA	Principal component analysis
pO_2	Partial oxygen pressure
PVE	Partial volume effect
RARE	Rapid acquisition with relaxation enhancement
RF	Radiofrequency
ROI	Region of interest
ROS	Reactive oxygen species
SEmax/60	Relative signal enhancement at maximum/60 seconds of enhancement
SER	Signal enhancement ratio
SPC	Supervised principal components
SNR	Signal-to-noise ratio
SPECT	Single photon emission computed tomography
T(1/2/2*)	Tissue relaxation times
T	Tesla
TE	Echo time
TIC	Time-intensity curve
TME	Tumour microenvironment
TOP	Time of peak intensity
TTP	Time to peak
TR	Repetition time
US	Ultrasound
VEGF	Vascular endothelial growth factor
Voxel	Volume pixel
WI	Wash in
WO	Wash out

Background

Cancer

Epidemiology

In 2012, the estimated number of new cancer cases worldwide was 14.1 million, and the corresponding number of cancer deaths was 8.2 million. In Europe, the corresponding numbers were 3.7 and 1.9 million cases. Cancer now causes more deaths than coronary heart disease or stroke, and WHO expects an increasing cancer burden over the next decades [1, 2].

Hallmarks of cancer

In 2000, Hanahan and Weinberg [3] proposed six distinctive and complementary biological capabilities, or hallmarks, that are acquired by normal cells during the multistep process that lead to the formation of malignant tumour cells and cancer development:

Sustained proliferative signalling

One of the most fundamental hallmarks is the capability of tumour cells to grow and divide (proliferate). In normal tissues, this process is carefully controlled by the production and release of substances that tells the cell to enter the growth-and-division cell cycle. Tumour cells acquire capabilities to *e.g.* produce their own growth substances or stimulate normal cells in the tumour microenvironment (TME) to support their proliferation [3].

Evading growth suppressors

Tumour cells must also evade the multiple, redundant and powerful programs constructed to suppress excessive cell proliferation, as well as the contact inhibition that supress further proliferation in normal cells when cell-to-cell contact is reached in dense cell populations [3].

Resisting programmed cell death

Another natural process that supports homeostasis in normal tissues is the programmed cell death by apoptosis. Apoptosis is triggered by *e.g.* physiological stress or DNA damage, whereby the cell is contracted, disassembled and removed by phagocytosis. The tumour cell avoids apoptosis in several ways, the most common being the loss of the TP53 tumour suppressor function, which is considered the guardian of the genome by its ability to detect and eliminate damaged DNA [3].

Enabling replicative immortality

Tumour cells must bypass the limitation of the number of cell growth-and-division cycles they can enter, which, in normal cells, is limited by the

shortening of the telomeres by each division. The telomeres protect the ends of the chromosomes, and when they are too short, chromosomal DNA is threatened and the cells enter apoptosis. In the majority of cancer cells, however, telomerase is present in abnormal levels. Telomerase is a specialized DNA polymerase with the capability to add telomere segments to the ends of the telomeres and thereby immortalize them [3].

Inducing angiogenesis

Tumours quickly outgrow the vasculature supporting tumour cells with oxygen and nutrients. The deprived tumour cells start signalling for blood vessel formation from existing vessels (angiogenesis) by releasing *e.g.* vascular endothelial growth factor (VEGF). VEGF bind to the surface of the endothelial cells lining the existing vessels, which in turn start proliferating to form the new vessels. In contrast to normal tissues, the pro-angiogenic signalling will continue in an uncontrolled fashion. This causes chronic cycles of sprouting and branching of the tumour vasculature and results in a highly chaotic and immature vasculature network of excessive branching, leakiness, shunts and micro haemorrhaging [3].

More than a decade later, some additional hallmarks have emerged, but the original six are still considered to provide a foundation for the understanding of the complex biology underlying cancer, and they are also widely investigated as targets for successful tumour treatment [4].

Tumour microenvironment and heterogeneity

Solid tumours are increasingly being recognized as complex tissues, in contrast to the earlier view of tumours as a collection of cancer cells of relatively homogeneous nature. A variety of cell types and subtypes constitute tumour stroma and parenchyma (tumour cells), but the interactions between the tumour and stromal cells are far from understood. Together, they constantly remodel the extracellular matrix according to their needs for growth and progression [5]. A complete understanding of the biology of the tumour thus requires the understanding also of the TME. Solid tumours typically comprise regions of high proliferative activity and reduced apoptosis, which result in increased cell density. On the contrary, the rapid growth and poorly organized and dysfunctional vascularization and blood supply result in regions with reduced proliferation, hypoxia and necrosis [4, 6, 7]. Furthermore, the microvasculature is often highly permeable and leaky, which in combination with poor lymphatic drainage and rapid growth within the encapsulated tumour volume contribute to an elevated interstitial fluid pressure (IFP) throughout the tumour. Typically, IFP is higher in central tumour regions, but rapidly normalize at the tumour edges [8-11]. Increased IFP and inadequate vasculature impedes the trans-capillary and

interstitial transport of oxygen and compounds such as nutrients and therapeutic agents to tumour cells [12-14]. Tumour cells in regions of hostile environment adapt by, *e.g.*, switching to anaerobic metabolism, and they progress to more malignant states by natural selection [5]. The heterogeneity imposes many challenges for therapeutic success, such as delivery of the therapeutic agents to poorly perfused regions, radioresistance due to hypoxia and regional response assessment.

This may also promote metastatic spread, since lactic acid is produced in large amounts under anaerobic metabolism, leading to acidification and loss of E-cadherin, which is important for cell-to-cell adhesion.

Neuroendocrine tumour (NET)

Neuroendocrine tumours (NETs) represent many different malignancies that arise from neuroendocrine cells in different parts of the body. Small intestine NETs are rare, but with significantly increasing incidence during the last decades [15]. The primary tumour is typically slow growing, but at the time of diagnosis, mesenteric, liver or more distant metastases are almost always present, resulting in inoperable disease. NETs are typically angiogenic and vascular, and express somatostatin receptors, which makes them suitable for imaging with radiolabelled somatostatin analogues, such as ^{111}In-octreotide, but also for therapy using *e.g.* ^{177}Lu-octreotate [16-18].

Tumour model

To study the effects of therapy on tumours, animal models are often used since it is possible to reduce the influence of genetic heterogeneity and environmental factors that complicate the interpretation of the results. Furthermore, analysis on cell cultures alone does not include the interaction of tumour cells with TME, and although the tumour does not grow in its original environment, it more closely mimics the human disease. Mice are advantageous since they are small, easy to handle during experiments, breed fast and have a well-known genome. In the present thesis, most studies were performed on Balb/c nude mice with xenografts from a human small intestine NET. This type of mouse is immunodeficient due to the lack of T-cells, which allows the tumours to grow. It is therefore a suitable animal to work with when analysing the effects of tumour therapy, especially when using MR equipment dedicated to small animal imaging.

Targeted radionuclide therapy

Surgery and/or radiotherapy are the only curative options for solid tumour cancers, but unfortunate locations of tumours or metastatic disease may make external radiotherapy or surgery impossible [19]. In targeted radionuclide therapy, a radionuclide is coupled to *e.g.* a peptide or an

antibody that bind specifically to the cells of the tumour. If the physical range of the radioactively emitted particle is well suited for the size of the tumour, only tumour cells and TME are irradiated, and side effects on nearby healthy tissue, that made external radiotherapy impossible, are reduced [18, 19].

Radiobiological effects on tissue

Ionizing radiation induces damage to DNA, either directly or indirectly via the production of reactive oxygen species (ROS), in addition to several other effects on intra- and intercellular signalling pathways, which optimally lead to tumour cell death [19]. Beside effects on DNA, other radiation-induced mechanisms can influence the curative effect, such as effects on protein or membrane integrity, but also effects that influence invasiveness and metastatic potential [19, 20]. Knowledge about radiobiological effects is based largely on external radiation therapy. The radiobiology of radionuclide therapy differs, *e.g*. due to inhomogeneous irradiation often including mixed fields, low absorbed dose rates and long exposure times, and must be further investigated in order optimize radionuclide therapy [19].

^{177}Lu-octreotate therapy

^{177}Lu-octreotate is primarily a beta emitting compound with great affinity for somatostatin receptors 2, 3 and 5, which has shown great promise for treatment of patients with inoperable NET disease regarding tumour regression, increased overall survival and improved quality of life, and it has shown little side effects [21, 22]. There are, however, few curative results reported, and few prognostic indicators for the individual patient. The high cure rates in animals transplanted with human NETs indicate that the treatment needs optimization, such as individualized treatment, radiosensitizing of tumour tissue, methods to increase receptor expression and combinations with other therapies, but with maintained or reduced normal tissue toxicity [18].

Therapy response assessment

The heterogeneity of tumours is probably one of the major reasons for therapeutic failures. Characterization of a cancer requires histological analysis of tumour biopsies and is critical for medical decision making, but biopsies are typically based on focally sampled regions [23]. Unfortunate biopsy sampling may therefore result in important diagnostic information being missed. Even if correct information is acquired, different tumours may respond differently to the same therapy. Ideally, tumour response would be evaluated early after onset of treatment. This would reduce costs, risks and unnecessary suffering due to inefficient treatment. To facilitate longitudinal follow-up, non-invasive assessment methods would be preferred. Imaging

can provide accurate measurements of tumour volume, but radiation therapy may not affect tumour size immediately, which makes assessments based on tumour size alone insufficient for early response assessment. Instead, the methods should be sensitive to early treatment-induced effects on the tumour cells, physiology, metabolism or TME [24]. Such methods would provide valuable guidance to suspicious tumour regions during biopsy for diagnosis, and provide surrogate markers for treatment-induced radiobiological effects during follow-up [25].

Imaging for therapy response assessment

Imaging has the advantage of offering an overview of the heterogeneous tumour, often in three dimensions. Several quantitative imaging techniques are already used clinically, and provide biomarkers reflecting structural, physiological and metabolic information of the tumour. Magnetic resonance (MR) imaging (MRI), single photon emission computed tomography (SPECT), scintigraphy using gamma camera, ultrasound (US) and [^{18}F]-2-fluoro-2-deoxyglucose positron emission tomography (FDG-PET) are some examples [26].

Scintigraphy and SPECT are imaging techniques that utilize the tumour specific uptake of certain radiopharmaceutical to image *e.g.* biological and metabolic changes in tumours [27, 28]. They are often used to complement other imaging techniques with higher spatial resolution in oncology. Several SPECT tracers are of interest for tumour imaging, such as apoptosis specific tracers based on annexin V [27].

PDG-PET utilizes the increased metabolism of tumour cells to accumulate the radioactive positron emitting nuclide ^{18}F in metabolic active tumours [25]. It is a sensitive tool for characterization of tumours and detection of metastases, and has *e.g.* been shown to detect changes in glycolytic rate in gastrointestinal stromal tumours already 24 h after Imatinib mesylate (Glivec) treatment, several weeks before effects were seen on tumour volumes [29]. However, the limited spatial resolution in PET makes it difficult to use as a single imaging modality.

Integrated systems combining *e.g.* metabolic information from PET or SPECT with computed tomography (CT) takes advantage of the morphological information gained from CT. PET/CT has provided synergistic effect *e.g.* in staging of lung cancer, where MRI is still challenging due to susceptibility effects [30, 31]. PET, SPECT and CT utilize ionizing radiation, which can be confounding in studies on effects of radiotherapy. PET imaging in highly energetic organs such as the brain, or close to locations of FDG accumulation such as in the pelvis around the

bladder is difficult due to the high background signal. Inflammation, often present in and around tumours, may also present increased glucose metabolism, which may reduce tumour specificity in PET imaging [32].

The synergistic value of the abovementioned techniques is largely dependent on proper alignment or fusion of images, which is often achieved by the hybrid systems available, such as PET/CT or MRI/PET where the imaged object remains in position during sequential acquisition using both modalities.

MR methods for response assessment

MR techniques provide images with unparalleled soft tissue contrast and excellent spatial resolution. Manipulations of the pulse sequences can also make the techniques sensitive to functional and physiological states and processes within the imaged tissue, such as blood perfusion, water molecular diffusion, metabolic composition and pH status, several of which are altered in tumour tissue, and affected by therapy [33]. MR thus offers a means to non-invasively probe different aspects of the tumour parenchyma and TME before, during and after treatment.

Until now, however, the potential of the MR methods is not fully explored, since tissue parameters derived from the MR methods are mostly evaluated as whole tumour average values, which does not account for intra-tumour heterogeneity. The non-invasiveness of the methods could also be better utilized, since it allows studies of the dynamical behaviour of the tissue parameters. Most importantly, evaluating the spatial and temporal variations of multiparametric MR information on tumour tissue in response to therapy would probably provide new insights into the biological meaning of the MR parameters, as well as the tumour biology. To our knowledge, few such studies have yet been performed. One application that would probably gain much from such evaluations is radionuclide therapy. As opposed to external radiotherapy, on which most radiobiology is built, radionuclide therapy is inhomogeneous, prolonged and may involve mixed radiation types. The inhomogeneity may be caused by differences in peptide or antibody uptake and availability due to inadequate vasculature [20, 34]. Methods to assess the tumour response to such therapies thus require the versatility offered by the proposed multiparametric MR methods. An introduction to the separate MR methods that will be included in this thesis is given below.

Diffusion weighted MRI

Diffusion weighted MRI (DWI) is a non-invasive imaging technique sensitive to the random motion of water, such as the Brownian motion of water molecules (diffusion), imposing an exponential attenuation of the MR

signal amplitude with increased diffusion sensitization (b-value). The apparent diffusion coefficient (*ADC*) can thus be quantified by fitting a simple mono-exponential model to the DWI signal with increasing b-value. On the timescale of a DWI experiment, the tissue water diffusion is restricted by the presence of *e.g.* cell membranes, which effectively reduces the attenuating effect of the diffusion sensitization on the MR signal. This makes DWI interesting for tumour treatment assessment, since higher ADC (less restrictions on water diffusion) would indicate reduced cell density and *vice versa*. However, capillary microcirculation within the DWI voxel, encompassing thousands of randomly orientated capillary segments, will mimic molecular diffusion on a macroscopic level, and impose an additional exponential attenuation on the MR signal, resulting in a positively biased diffusion measurement. The intravoxel incoherent motion (IVIM) model [35] treats tissue water molecular diffusion (*D*) and perfusion related "pseudo-diffusion" (*D**) as two separate compartments. IVIM-DWI thus allow quantification of both these phenomena separately, in addition to the fractional contribution of *D** to the signal decay with increasing b-value, referred to as the perfusion fraction (*f*). The IVIM model thus provides a means to quantify *D* (*ADC* without perfusion bias) and perfusion related effects non-invasively, without the use of contrast media injection. Both the ADC and IVIM models are obviously simplistic since there are probably more than just two distinct compartments of incoherent motion in tissues that affect the diffusion weighted MR signal, and more advanced models exist (e.g. [36]). However, the two compartments described here are probably the most influential on the MR signal measured *in vivo*, outside the brain, where *e.g.* motion signal-to-noise ratio (SNR) and susceptibility effects impose limitations on the quality of the measured signal and the complexity of the models applied.

Considerations regarding bi-exponential model fitting

The IVIM model is bi-exponential, which makes it more prone to errors introduced by the model fitting algorithm compared with mono-exponential models such as the ADC model. In tumours, there are likely regions with low perfusion fraction, which essentially makes the bi-exponential model over-parameterized, which may in turn yield unstable results. Several methods have been proposed as alternatives to the least squares fitting methods commonly applied to estimate IVIM parameters. Bayesian model fitting has been proposed as a robust alternative [37]. Barbieri et al. [38] compared several model fitting strategies commonly found in the literature, including the most common least squares and stepwise methods, and demonstrated the superiority of the Bayesian in this context. Bayesian methods require an *a priori* distribution of the model parameters before fitting. Commonly, a non-informative and truncated uniform or reciprocal

prior distribution is used. A shrinkage prior was suggested to improve the fitting of D*, which often results in noisy estimates [39]. The output of a Bayesian model fit is a marginalized probability distribution of each parameter, as opposed to the point estimates resulting from least squares fitting. Thus, a measure of *e.g.* central tendency is required in order to make the results more comprehensible. Both mean, median and mode values have been used to describe the central tendency in the context of Bayesian model fitting [37, 39, 40]. The choice of prior distributions and central tendency representation is of particular importance in the low SNR setting, characteristic of diffusion weighted imaging, and the alternatives should be evaluated in order to optimize the parameter estimates.

DWI is a generally accepted oncological imaging technique *e.g.* for differentiating benign from malignant lesions or monitoring radiation treatment response. It is simple to use and does not require endogenous contrast media, which enables its use in patients with impaired renal function [41].

In the research setting, evidence suggests that *ADC* has a great potential as a surrogate marker for tumour control, and for indicating response very early after treatment. For example, early increases in mean *ADC* was observed in liver cancers in patients receiving radiotherapy, and correlated with higher doses and sustained tumour response, whereas size measurements such as volume changes on T2 weighted images or monitoring of the largest tumour diameter did not [42]. In a mouse model of prostate cancer, *ADC* was successfully used to differentiate well differentiated adenocarcinoma from poorly differentiated carcinoma and normal prostate tissue, and cancer development could be predicted by locally reduced *ADC* before changes in median whole prostate *ADC*, nor alterations in prostate volumes were detected [43].

Due to recent technical advancements in *e.g.* gradient systems, however, efforts to apply IVIM analysis are currently increasing [32]. In a recent study, where IVIM-DWI was used to assess the efficacy of a vascular disruptive agent in a rabbit VX2 liver tumour model, f and D^* showed statistically significant decreased values already at 4 h post-therapy, and D showed a statistically significant increase at 24 h. Furthermore, the decreasing f and fxD^* (a quantity reflecting blood flow), were correlated with lower tumour volume progression during a one-week follow-up, and comparisons with histology demonstrated statistically significant and positive correlations between f and fxD^* and micro-vessel density and between D and necrotic tissue fraction [44]. The use of IVIM-DWI should also increase the sensitivity of measurements of diffusion related tumour

characteristics. For example, Rijswijk *et al.* [45] compared *D* and *ADC* in soft tissue tumours in patients with different types of tumours, and in different locations, and found that *D* could separate malignant from non-malignant tumours, whereas *ADC* could not.

In an IVIM-DWI study of a mouse mammary carcinoma model a statistically significant, positive correlation between *fxD** and interstitial fluid pressure (IFP) was found, which makes IVIM-DWI an interesting alternative to the invasive techniques previously required for IFP measurement [46].

Dynamic contrast enhanced MRI

Neo-vascularisation is critical for tumour growth, and driven by angiogenic factors that are expressed due to hypoxia [47]. The newly formed vessels are highly permeable, which cause low molecular weight contrast agents to leak into the extracellular extravascular space (EES). Dynamic contrast enhanced MRI (DCE-MRI) exploits this leakage by measuring the concentration of contrast agents, and hence the signal enhancement caused by shortened T1 relaxation, in the EES. It can thereby provide biomarkers of hypoxia, and it is widely used clinically for early evaluation after anti-angiogenic therapies [25, 47]. It provides important information on tumour properties that affect delivery of therapeutic agents to the tumour cells, such as the tumour spatial distribution of vascularity, local vessel structure and function, perfusion, diffusivity in the EES and blood volume [48, 49]. Since these properties may vary throughout the tumour, and thereby in part explain the heterogeneous response of tumour therapies, the DCE-MRI signal time-intensity curve (TIC) has been extensively studied using both semi-quantitative and quantitative approaches, and it provides spatially resolved imaging biomarkers of relevance to therapy [25, 50]. For example, the tumour uptake of radionuclides in a rat model of pancreatic cancer correlated with semi-quantitative DCE derived parameters reflecting exchange rate between blood plasma and EES [50]. In a rat model of prostate cancer, tissue oxygenation measured using pimonidazole stained tissue sections correlated with TIC behaviour; fast changes in the TIC correlated with adequate perfusion, whereas slow changes were found in hypoxic regions [51]. It has further been suggested that DCE-MRI may provide biomarkers for IFP, which is associated with clinical outcome in many types of cancers [52-54].

Relaxation MRI

A driving force of the development of MRI was the discovery that tumours had shorter *T1* relaxation time than most normal tissue. *T1* describes the recovery of longitudinal magnetization after excitation by an RF pulse, and it is shortened by the presence of macromolecules. *T1* should thus be

influenced by treatments affecting the molecular content of tumour tissue water. A study using anti-angiogenic therapy of an ovarian tumour mouse model showed a statistically supported increase in *T1* already 2 days after onset of therapy, and it was still increased after 14 days [55]. In a study on patient with glioblastoma, T1 could be used to predict tumour progression [56].

Transversal decay of magnetization after excitation is described by the T2 relaxation time. T2* is the corresponding constant if no spin echo is used to re-phase the signal decay due to magnetic field inhomogeneity. Deoxyhaemoglobin is paramagnetic and the local magnetic field around blood with low pO_2 may be affected, which in turn would reduce T2* and hence the MR signal. Tumour vessel abnormalities, hypoxia and haemorrhage could thus have an effect on the T2* value. In patients with colorectal liver metastases, pre-treatment T2* has been associated with overall survival [57].

Aims

The overall aim of this thesis was to investigate the potential of multiparametric MR methods for prediction and assessment of tumour therapy response, based on an animal model of neuroendocrine tumour and treatment using ^{177}Lu-octreotate.

The specific aims were:

- to study the possibility to use MRI methods to accurately determine the volume of small tumours in a limited acquisition time (**I**),
- to improve the IVIM-MRI parameter estimates by optimizing the choices of model fitting algorithms and parameters (**II**),
- to study the relations between tissue parameters derived from multiple MR methods and parameters derived from histological analyses of the corresponding, spatially registered tumour sections (**III**),
- to investigate how multiple MR parameters available for response assessment are associated with response of neuroendocrine tumours receiving radionuclide therapy (**IV**), and
- to propose potential MR derived imaging biomarkers for therapy response assessment (**III & IV**).

Methods

General experimental setup

Animals and tumour models

This thesis is mainly based on studies on female BALB/c nude mice (Charles River, Japan and Germany) with xenografts of a human small-intestine NET (GOT1 [58]) growing subcutaneously in the neck region since the age of four weeks. Animals were housed in a pathogen-free environment receiving standard diet and water *ad libitum* (**I-IV**). At the start of the MR experiments, tumour diameters were between 10 and 20 mm (**II-IV**).

Ethics

The Gothenburg Ethical Committee on Animal Research approved the studies.

MR system

All MR experiments were performed on a 7T MR system equipped with water cooled gradients of maximum 400 mT/m (Bruker BioSpin MRI GmbH, Germany; software: ParaVision 5.0 (**I**) or 5.1 (**II-IV**)). RF signal transmission and reception was achieved using a 72-mm volume coil and an actively decoupled, 4-channel array rat brain coil, respectively, or a 50-mm quadrature transmit/receive volume coil (RAPID Biomedical GmbH, Germany).

Animal positioning, anaesthesia and monitoring

Animals were imaged either in prone position using respiration triggered acquisitions or in supine position without respiratory triggering, but with tumours immobilized in a hole cut out from the supporting bed. For the latter setup, gel (Lectro Derm, Handelsvaruhuset Viroderm, Sweden) was used to improve the magnetic field homogeneity within the tumour, and the 4-channel receiver coil was mounted under the tumour. A pressure sensitive pad (SA Instruments, Inc., NY, USA) placed next to the animal provided the signal for respiratory triggering, and was used for respiration monitoring during all acquisitions. Anaesthesia was maintained during acquisitions using a gaseous mixture of air and isoflurane (1.5-3.0 %).

Figure 1 illustrates the setup used for most experiments in **II-IV**, and Figure 2 states the animal positioning and coils used for the different experiments.

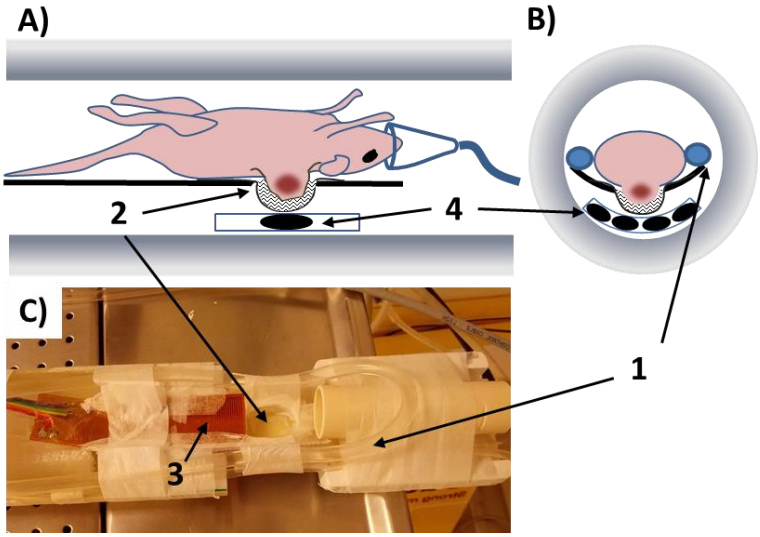

Figure 1. The position of the animal in the magnet bore during acquisition (A), with cross-sectional view in the level of the tumour (B), and custom made animal holder (C). This setup was used for the animals imaged in supine position without respiratory triggering (n=18, included in **II-IV**). The tumours were immobilized in a hole cut out from the supporting bed (arrows marked with 2). The magnetic field homogeneity within the tumour was improved by submerging the tumour in gel, and thereby offsetting the tissue-air interface. The gel was confined by a thin plastic film separating the gel from the elements of the 4-channel receiver coil (4) by only a few mm. Body temperature was maintained using an electrical heating pad (3) under the animal and a circulating warm water system set to 40°C (1). Isoflurane gas for anaesthesia was delivered via a nose cone or a tube. The pressure sensitive pad used for respiratory monitoring is not shown

MRI for tumour volume assessment (I)

The accuracy of tumour volume estimations based on MRI was evaluated by comparing tumour volumes determined from T2 weighted images with the weight of the resected tumours. Both 2- and 3-dimensional (2D, 3D), fat suppressed, rapid acquisition with relaxation enhancement (RARE) sequences were acquired, with varying image resolution (matrix size). The volume estimates were based on manual delineations of the tumours and multiplication of the total number of tumour voxels by the voxel volume. The reader is referred to **I** for the detailed description of image acquisition parameters, intra- and interobserver variability, partial volume effects and comparisons with standard, gauge block based volume estimates.

MR experiments (II-IV)

Localization and shimming

A fast gradient-echo localizer (a.k.a. tripilot) was used for verification of correct tumour position (magnet isocenter), and for geometric planning of additional experiments. Optimization of field homogeneity was achieved by shimming based on a field map acquisition (Bruker MAPSHIM macro). The full–width-at-half-maximum was measured on the water spectral peak of a voxel within the tumour, and the shim procedure was repeated until it reached a minimum, or below 40 Hz (0.13 ppm).

Imaging protocols

One day prior to therapy (day -1), animals were subjected to multiparametric MR experiments. After tripilot acquisition and shimming, the IVIM-DWI was acquired. The FOV and slice locations were exported and used also for the subsequent T2* mapping, T1 mapping and DCE-MRI (central slice only). During the sixth dynamic acquisition in the DCE-MRI series, contrast agent was injected via a catheter inserted into a tail vein, with infusion line reaching outside the magnet bore. For this, a 0.1 M, 0.3 mmol/kg bodyweight, Gd-DTPA (Dotarem, Gothia Medical, Sweden) solution was used. The T2 weighted MRI experiment was acquired without slice gaps and with increased number of slices for complete tumour coverage. The total experiment time, including preparation, was typically less than 1.5 h per animal. The experiments were repeated on days 1, 3, 8 and 13 after treatment (day 0), but DCE-MRI was not performed on day 13. Figure 2 shows a timetable of the imaging experiments and the treatment. The detailed acquisition parameters can be found in Table 2 of **IV**.

Treatment & radiopharmaceutical

An injection of 15 MBq ^{177}Lu-octreotate (IDB Holland, the Netherlands) was given in a tail vein on day 0. The radiopharmaceutical had been prepared according to instructions from the manufacturer, resulting in a specific activity of 26 MBq/µg octreotate. The fraction of peptide-bound ^{177}Lu was > 98 %, as determined by instant thin layer chromatography (ITLC™ SG, PALL Corporation, USA), with 0.1 M sodium citrate (pH 5; VWR International AB, Sweden) as mobile phase. The ^{177}Lu activity in syringes before and after injection was measured by a well-type ionization chamber (CRC-15R; Capintec, IA, USA). The extrapolated absorbed tumour dose was estimated to approximately 4.0 Gy, as previously described [59]. The amount of ^{177}Lu-octreotate was chosen to result in only partial tumour remission.

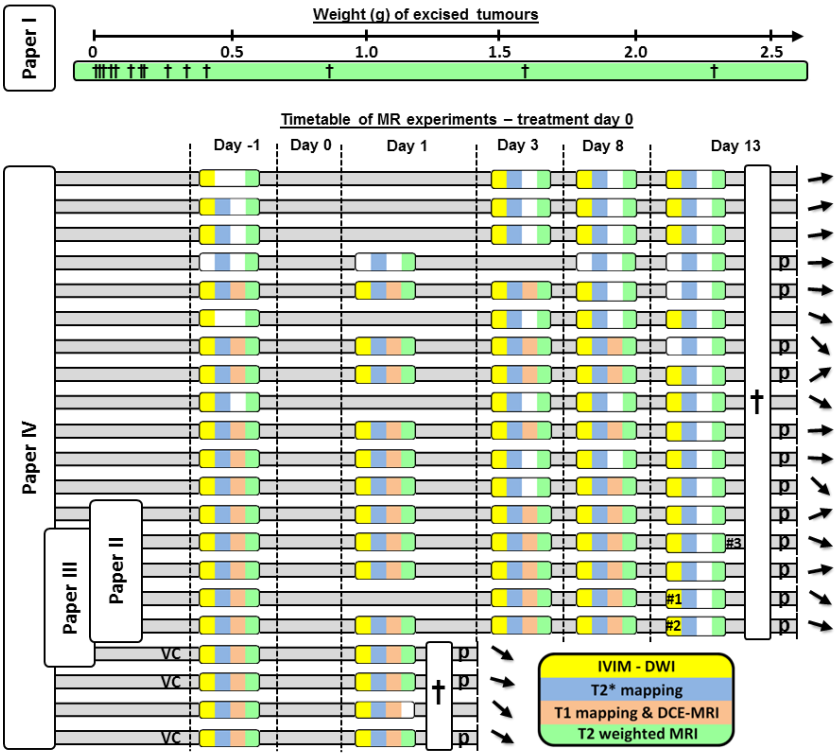

Figure 2. Overview of the imaging experiments and animals. Upper pane (included in **I**): The crosses on the green bar mark the different weights (at resection) of the 15 tumours that had their volumes successfully determined from 2D, T2 weighted MRIs acquired before resection. These animals were imaged in prone position using the surface coil and with respiratory triggering. Lower pane: Imaging and treatment schedule for the 21 animals used in **II**-**IV**. Colours indicate which MR methods were applied (*cf.* figure legend, white = not acquired). These animals were imaged in supine position according to the setup explained in Figure 1, except for three animals which were imaged using the volume coil (indicated by VC), in prone position and with respiratory triggering. Animals were killed and tumour tissue was harvested for proteomics and histological staining after the day 1 or day 13 imaging experiments (white bar with black cross). p = samples for proteomics taken from peripheral and central tumour tissue. The angle of a black arrow (relative to a horizontal line of angle 0) indicates the relative tumour volume development until day 8 (proportional to the response variable). #1 and #2 indicate the IVIM-DWI experiments corresponding to tumour example 1 and 2, respectively, shown in Figures 7 and 8. Heat maps of #3 are shown in Figure 9

Tissue harvesting

After the final MR experiments, animals were given a lethal *i.p* injection of sodium pentobarbitone, followed by cardiac puncture. Either the tumour was immediately removed and weighed (**I**), or it was divided and marked for subsequent image registration (**III**) and protein expression analysis (**IV**). Figure 3 describes the procedures of tissue harvesting used in **III-IV.**

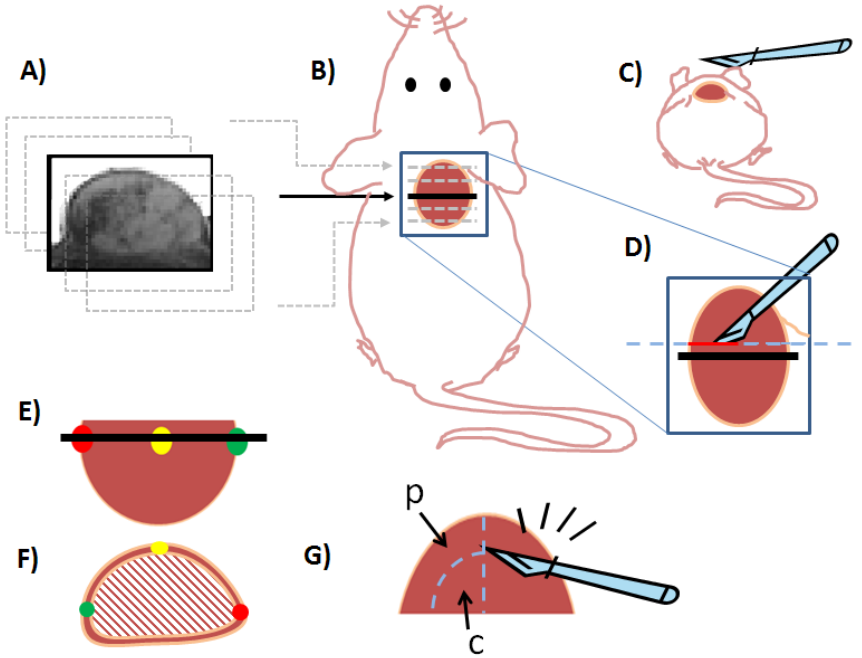

Figure 3. Tissue harvesting for histological staining, image registration (**III**) and proteomics (**IV**). After the final MR image series had been acquired, the animal was killed and placed in prone position on an operation table (B-C). The most central, T2 weighted image of and MRI series is shown (A), with arrows indicating the tumour sections that were imaged (A-B). The central image position is also shown by the black, solid line (B, D and E). An incision was made through skin and tumour in a plane parallel to the central image section (D, dashed, blue line). The imaged section was marked by injecting small amounts of green, yellow and red tissue ink on the right, dorsal and left tumour boarder, respectively (E). The tumour half containing the ink was prepared for histological staining. In the microtome, the cut surface was placed to face the microtome knife sweep plane, and once the tissue ink was visible (F), the histological sections were collected, stained, digitalised and registered to the MR images (**III**). The other tumour half (G) was further divided into central (c) and peripheral (p) parts for protein expression analysis (**IV**)

Post-processing

Software

Post processing such as image filtering and model fitting, as well as statistical calculations, were performed on PC workstations using MATLAB (R2008b (**I**), R2014b (**II**), R2015b (**III-IV**), The MathWorks, Inc., USA) unless otherwise stated. Both MATLAB standard and in-house developed scripts and graphical user interfaces were used, and relevant MATLAB functions will be stated in the text. For additional details, the reader is referred to the corresponding separate papers included in this thesis.

Optimization of IVIM-MRI model fitting (II)

To optimize the quality of the IVIM model parameters for the experimental setup and tumour model used in the present studies, both *in vivo* data from the IVIM-DWI experiments and computer simulations were used to estimate the parameters. Bayesian methods with three different *a priori* distributions (reciprocal, shrinkage and uniform) and three different representations of central tendency of the resulting parameter distributions (median, mean and mode) were evaluated. The SNR in tumour in the *in vivo* images (b=0) was calculated (resulting in SNR ~ 15-25), and different levels of Rician noise were added to the simulated parameters to evaluate performance on similar SNR levels (SNR = 10, 20 and 40 were simulated). The diffusion *b*-values and parameter limits used for IVIM-DWI were used also in the simulations.

Calculation of MR parameters (III-IV)

A 2x2 median filter was applied to all images before further post-processing and parameter calculations. The parameters derived from MRI examinations can be found in Table 2 of **IV**. Briefly, IVIM-DWI parameters were estimated using a Bayesian model fitting method with uniform prior distribution, whereas other model parameters were fitted using least squares methods. DCE-MRI parameters were semi-quantitatively determined by analysing the MR signal time-intensity curve after contrast injection.

Histology, image registration & data sampling (III)

Histological imaging (III)

The microtome produced 2-3 µm thick tumour sections of the tumour half prepared for histological analysis (Figure 3), and sets of four sections were collected for histological and immunohistochemical staining. One section was stained with haematoxylin-eosin (HE) using Tissue-Tek Prisma (Sakura FineTek, Sweden), another section was stained with Masson Trichrome (MT) using Artisan Link (Dako, Denmark). Two other sections were processed for immunohistochemical staining. They were pre-treated with EnVision™ FLEX Target Retrieval Solution (high pH; PT-Link; Dako, Denmark) followed by incubations using Envision Flex (Dako, Denmark). As primary antibodies, Ki67 (AB9260; Merck Milipore) and CD31 (AB28365; Abcam, UK) were used. The staining was performed in an Autostainer Link (Dako, Denmark) following the manufacturer's instructions. In each run, positive and negative controls were included. A Leica SCN400 Slide Scanner (40x magnification, Leica Microsystems, Germany) was used to digitalize the stained sections. The resulting high resolution histological images (0.25 x 0.25 μm^2) were exported for further processing on a PC workstation.

Spatial registration of MR- and histological images (III)

Spatial registration of MR images, parameter maps derived from MR images and the histological images was performed for the tumours where the quality of histological sections and MR images/maps were satisfactory. Artefacts in parts of images, or lack of visual landmarks were handled by avoiding registration of the entire tumour in a single step. Instead, registration was performed sequentially on tumour sub-regions, and when data had been extracted (sampled) from an entire sub-region, another sub-region was registered and sampled.

Data sampling (III)

Data samples were collected by 1) automatically creating a 250 x 250 μm^2 region-of-interest (ROI) within a registered tumour sub-region, 2) calculating the HE index (see below) for the ROI, 3) sequentially transforming the ROI coordinates to corresponding positions on the other registered images for index calculation or extraction of the ROI mean MR parameter value and, 4) automatically translating the HE ROI coordinates for sampling of an adjacent position within the sub-region. Steps 2-4 were repeated until the entire sub-region was completely sampled. If another tumour sub-region could be registered, it was sampled according to steps 1-4, and the process was repeated until as much of the tumour area as possible had been sampled.

Definition of histological indices (III)

The ROI index for apoptotic activity was calculated by using a cell segmentation method based on previously presented principles [60] combined with colour thresholding. It was designed to detect cell shaped objects (round to oval), and the colour thresholds were used to identify only the tumour cells with dark stained nuclei. The apoptotic tumour cell count (HEcount) could thus be defined as the number of apoptotic cells per 250 x 250 μm^2 surface area, under the assumption that a dark stained nucleus represented a cell with condensed chromatin due to apoptosis (*cf.* [61]). The Ki67 index was determined similarly, but on Ki67 images the colour threshold was set to detect only cells with brown stained Ki67 positive chromatin. Proliferating tumour cell count (Ki67count) was thus defined as the number of Ki67 positive cells per 250 x 250 μm^2 surface area. Figure 4 illustrates the method for cell segmentation.

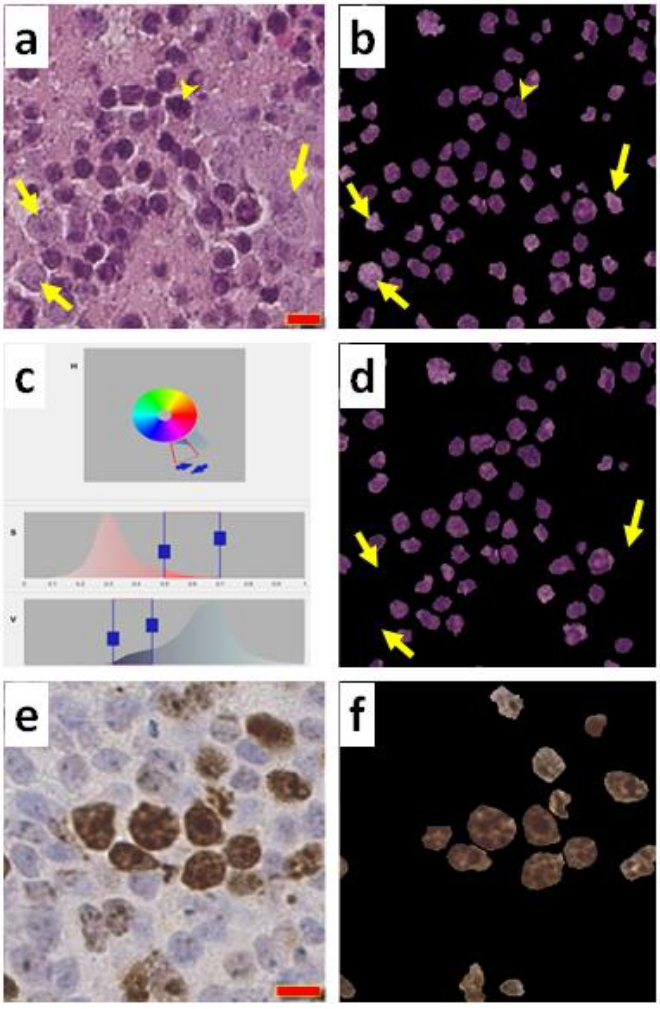

Figure 4. Tumour cell segmentation in HE (a) and Ki67 (e) stained histological sections of one of the studied GOT1 tumours. In (a), a yellow arrow head points at a tumour cell where the dark stained (HE positive) nucleus indicates condensed chromatin, typical of apoptotic cells. Arrows point at tumour cells not regarded apoptotic. In (b), the same image region is shown after automatic cell segmentation. Clearly, both apoptotic (arrow head) and non-apoptotic (arrows) are detected. By applying an additional filter based on manual adjustment of colour thresholds (c, screen capture from MATLAB colour segmentation application), the cells without a dark stained nucleus could be rejected (d), whereby the remaining, apoptotic cells could be automatically counted. The same procedure was applied to the Ki67 magnification in order to calculate proliferating, Ki67 positive tumour cells only (brown stained cells in e-f). Red bars indicate ~10 µm

Micro-vessel density (MVD) and fibrotic density (FD) were defined as the fraction of CD31 and MT positive area per 250 x 250 μm^2 surface area, respectively. These indices were determined by colour thresholding only (Figure 5).

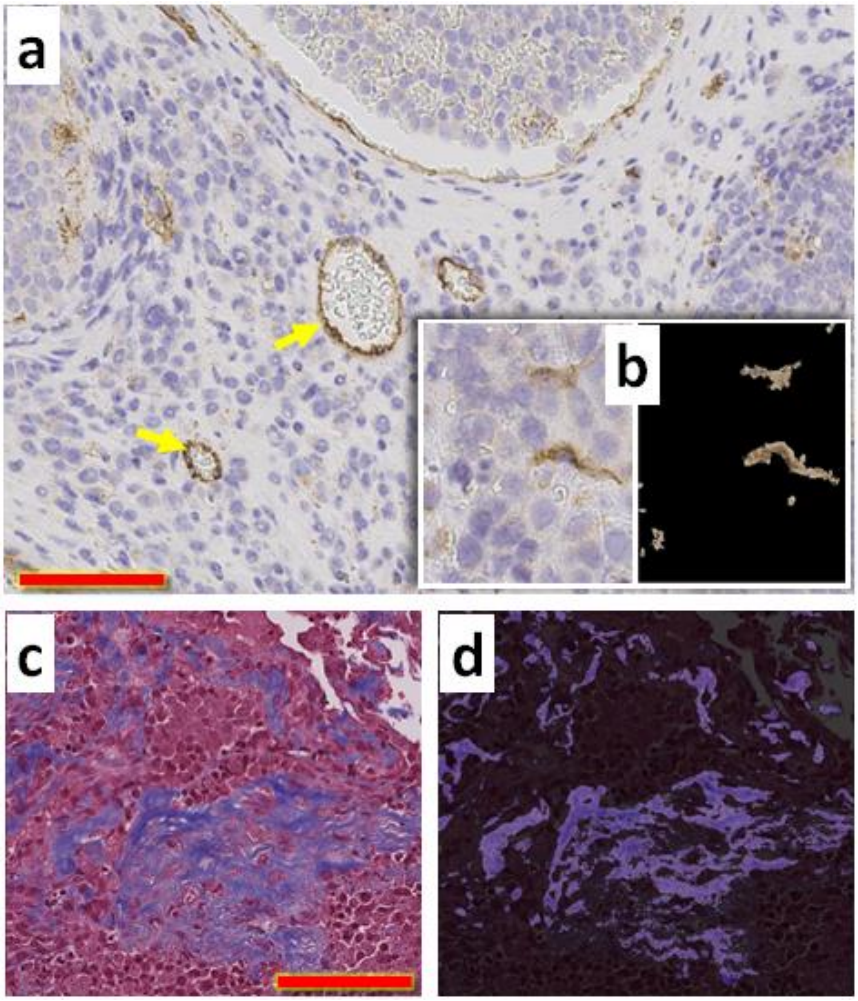

Figure 5. Vascular endothelial cells lining the vessels in one of the studied GOT1 tumours are stained with CD31 (a, brown stain), and colour segmentation has been applied for calculation of micro-vessel density (magnification in b). Yellow arrows point at relatively large vessels surrounded by endothelial cells stained brown by CD31, where erythrocytes are visible within the vessels. In (c), Masson Trichrome stains fibrotic tissue blue, and the same region is shown in (d) after colour segmentation for calculation of fibrotic density. Red bars indicate ~100 µm

The segmentation of apoptotic and proliferating tumour cells and the colour thresholds used to determine MVD and FD were validated by a board certified pathologist before data extraction.

Response verification (IV)

The change in tumour volume after treatment was used to define response. Tumour volumes were determined from the T2 weighted images of each experiment, as described above and in **I**, and the linear regression coefficient of the relative tumour volumes (from day -1 to 8) constitutes the response variable. It should be noted, therefore, that a greater tumour volume regression after treatment corresponds to a lower value of the response variable, and *vice versa.*

Spatial and temporal evaluation of MR features (IV)

MR parameters (*e.g.* ADC) were evaluated both as representing tumour median values, and as representing median values of a particular tumour region only (*e.g.* central or peripheral tumour). In this study, annular discs shaped like the tumour were constructed, and data were extracted from regions covered by these discs. Figure 6 illustrates the construction of discs and extraction of data. Data were extracted from the tumour section covered by the single slice DCE-MRI experiment. For improved statistics of the other experiments, however, data from the two most adjacent slices (in total three slices) were also extracted, and merged with central slice data before evaluation. The efficacy, or importance, of the MR parameters regarding response assessment, was evaluated for the tumour and the five discs separately. Furthermore, both the pre-treatment (day-1) MR parameter values and the change in values over time after treatment were evaluated.

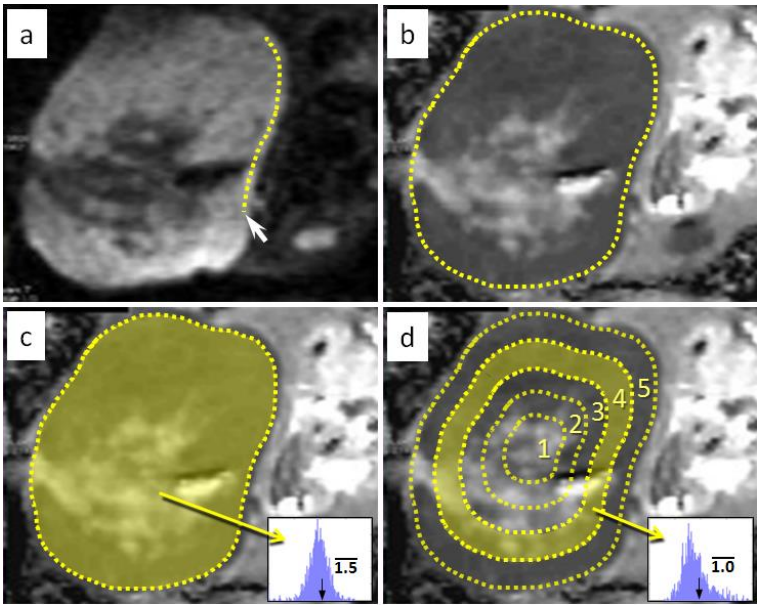

Figure 6. Illustration of the extraction of tumour and regional median MR parameter values of a subcutaneous GOT1 tumour. The central slice of the DWI experiment (b=800 s/mm^2) is used for tumour delineation (a). The resulting ROI is transferred to the ADC map (b) and the median value of the distribution of ADC values within the ROI is extracted (c). Four additional identically shaped ROIs, with stepwise decreased radius, are automatically reproduced (d), which separates the tumour into five regions. The central region is designated disc 1, and the annular disc shaped regions are designated discs 2-5 (d). Extraction of ADC data from disc 4 is shown in (d), revealing lower median diffusion (1.0 μm^2/ms) in this tumour region compared with the overall median diffusion (1.5 μm^2/ms) of the tumour (fictional diffusion data)

Definition of MR features (IV)

Henceforth, an MR feature is the median value of a particular MR parameter in a disc or in the tumour before treatment (day -1), or the change in the corresponding median value from day A to day B (designated A:B or Δday A:B). The following combination of days were evaluated: A:B = -1:1, -1:3, -1:8, -1:13, 1:3, 3:8 and 8:13. Furthermore, two models of change were evaluated: *absolute* change [value(B) - value(A)] and *relative* change [value(B) - value(A)] / value(A).

Proteomics (IV)

Samples were taken from central and peripheral tumour tissue in 15 tumours (Figure 2). The samples were prepared and analysed using liquid chromatography tandem mass spectrometry (LC-MS) with tandem mass tagging as described in **IV** and [62]. Detected proteins were associated with biological functions using the Gene Ontology database (http://www.geneontology.org) [63].

Data handling and statistics

Associations between MR parameters and histological indices (III)

Since samples were taken from five different tumours, where random effects may be present due to *e.g.* tissue preparation, colour threshold levels or coil combination, the underlying pairwise associations between MR parameters and histological indices were evaluated using linear mixed-effects regression analysis. The level of redundancy in the information provided by the investigated MR parameters was evaluated using agglomerative hierarchical clustering.

Prior to analysis, non-normally distributed parameters were transformed using the Box-Cox power transformation (Matlab *boxcox* function), and pairwise deletion was used to account for missing values in the pairwise comparisons. A regression coefficient was considered significantly different from zero for $p < 5.0 \times 10^{-4}$ (0.05 adjusted for multiple comparisons using the Benjamini & Yekutieli method ($q = 0.05$)).

Feature selection (IV)

Prior to feature calculations, non-normally distributed MR parameters were transformed using the Box-Cox power transformation and standardized to mean value = 0 and standard deviation = 1. Thereafter, features were defined, and only those with less than 50 % missing values were analysed. Data imputation was used to replace missing values in the remaining features, where imputed values were stochastically selected from a normal distribution.

The relative importance of each feature regarding response assessment was evaluated using the least absolute shrinkage and selection operator (lasso) feature selection method [64], preconditioned to better handle the high number of features using the supervised principal components (SPC) method [65]. The lasso returns the linear regression coefficient (β) of selected features, where a higher β magnitude thus indicates higher importance.

Since many of the included features would most likely be highly correlated to each other (*e.g*. from adjacent discs), and since the lasso is prone to arbitrarily select only one of two highly correlated features, the imputation and feature selection process was repeated 5000 times. The β-coefficients of returning features were cumulatively added, thus yielding a feature specific β-sum which could be related to the other features β-sums.

Proteomics (IV)

The evaluated protein quantity was the individual tissue sample protein amount normalised to the mean amount of the protein in all tissue samples. Non-normal protein distributions were transformed using the Box-Cox power transformation. Only proteins that were linearly correlated with response with high statistical significance (p-values < 0.01) were analysed. These proteins were evaluated for correlations with the MR-features with high β-sums. Pearson correlation coefficients are stated, with corresponding p-values derived from Student's t distribution under the null-hypothesis of no correlation at all. Multiple comparisons were corrected for using the Benjamini & Yekutieli method ($q=0.05$).

Results

MRI accurately predicts tumour volume (I)

The results in **I** showed that volumes determined from both 2D and 3D sequences were highly correlated with tumour weight at resection. 3D acquisitions with 160^3 μm^3 voxels yielded regression coefficient (r) = 0.94 and goodness-of-fit $R^2 = 1.00$. Evaluating small tumours only (volume < 0.2 g, n = 10) yielded: r = 0.90, $R^2 = 0.98$. Partial volume effects were negligible for the range of tumour volumes (Figure 2) and voxel sizes investigated. Acquisition times were drastically reduced when using larger voxels, with *e.g.* the smallest tumour (0.01 g) requiring 55, 34 and 22 minutes for acquisitions using 160^3, 200^3 and 240^3 μm^3 voxels, respectively. 2D acquisitions (slice thickness = 700 μm, in-plane resolution ~150 x 200 μm^2) and 3D acquisitions yielded similar correlations (volume < 0.2 g: n = 9, r = 0.94 and R^2 = 0.96), but with the advantage of only a few minutes acquisition time for the 2D method. Interobserver variability was, however, increased for tumour volume delineation in 2D images (Table 2 in **I**).

^{177}Lu-octreotate induced tumour volume changes (IV)

The 15 MBq ^{177}Lu-octreotate treatment resulted in a range of tumour volume responses, from tumours shrinking to less than 50 % of baseline volume during the first week of follow-up, to tumours that almost showed similar growth kinetics as untreated GOT1 tumours (~two-week doubling time). After one week, practically all tumours showed increasing volumes again. Figure 2 in **IV** shows the therapeutic effect on individual tumour volumes of the 21 tumours studied in **II-IV**. The linear regression coefficient of the relative tumour volumes (from day -1 to 8), *i.e.* the response variable, is indicated for each tumour in black arrows in Figure 2.

Optimal method for Bayesian IVIM-MRI parameter estimation (II)

Examples of parametric maps from Bayesian model fits to data acquired *in vivo* are shown in Figure 7, with corresponding parameter distributions summarized in Figure 8.

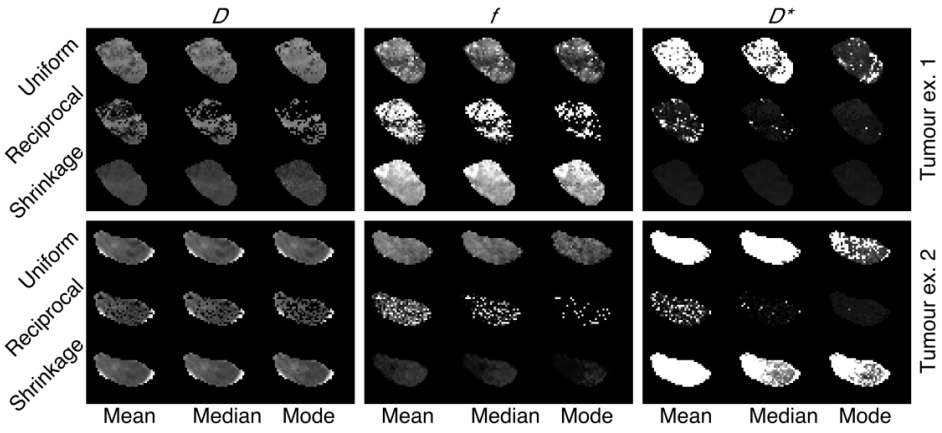

Figure 7. Parameter maps of *D*, *f* and *D** of a single tumour section constructed using different combinations of prior distribution (uniform, reciprocal and shrinkage) and central tendency measure (mean, median and mode) and for two of the five tumours analysed in **II**. Both tumours had an initial size of approximately 600 mm^3, and responded similarly to therapy (*cf*. Figure 2). The display ranges are *D*: [0 2] $\mu m^2/ms$, *f*: [0 0.4] and *D**: [0 50] $\mu m^2/ms$ (adapted from **II**)

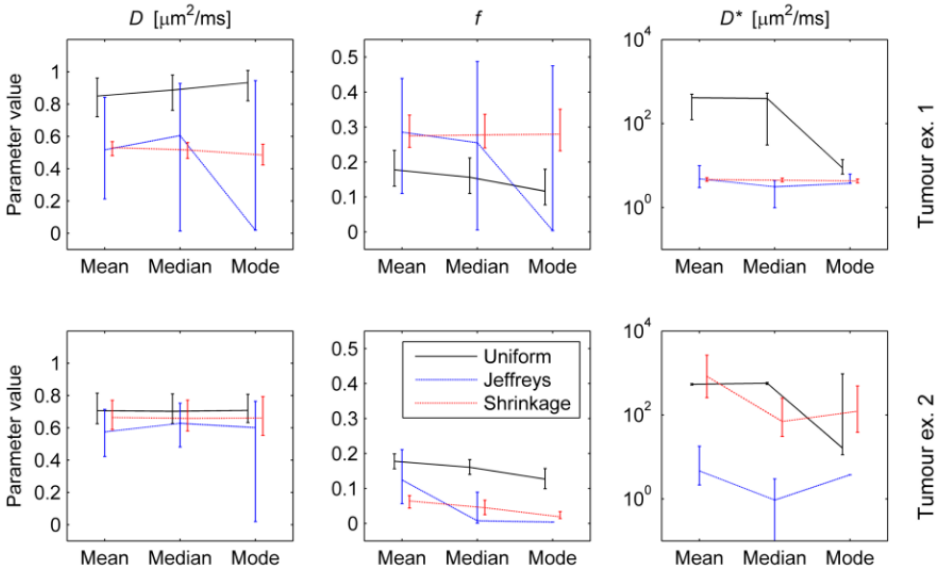

Figure 8. The distribution of the parameters displayed in Figure 7 are shown using the upper, middle and lower quartile (adapted from **II**)

Visual inspection of the parametric maps of *D*, *f* and *D** reveal that the reciprocal prior results in noisy estimates for most combinations of parameters and measures of central tendency (Figure 7). This is confirmed by the magnitude of the error bars for the reciprocal prior in Figure 8. The shrinkage prior resulted in less noisy parameter maps (Figure 7), with narrow distribution (Figure 8), but yield either high *f* or low *D** or *vice versa* in the two example tumours. When comparing parameters from all five tumours, the uniform prior seems to vary less regarding the absolute level of the parameters (partly shown by the two examples in Figure 8). In general, the choice of central tendency affected the absolute level of the parameters, but most often only to a small extent (partly shown in Figure 8). Of the priors assessed, the uniform prior yielded the most stable results, but combined with mean or median representation it tended to give little or no information on the *D** parameter (Figure 8).

In general, the results from the simulations were in agreement with the *in vivo* results, and are further evaluated in **II**. In brief, the estimation error (difference between estimated and simulated value) for *D* with uniform prior was symmetrically distributed around zero, whereas the reciprocal prior induced a bias. For small simulated *f*, estimated *f* was slightly overestimated by the uniform prior combined with mean and median representations, whereas mode showed no such trend. With a reciprocal prior, *f* was severely underestimated for all measures of central tendency, particularly for mode representation at low SNR.

MR parameters reflect important tumour biology (III)

Histological heat maps show tumour heterogeneity (III)

The combination of the algorithm for cell detection and colour thresholding resulted in adequate identification of apoptotic cells in the HE images and proliferating cells in the Ki67 images (Figure 4). Fibrotic tissue and vascular endothelial cell presence were also adequately identified in the MT and CD31 images, respectively (Figure 5). Heat maps of the histological indices HEcount, Ki67count, MVD and FD revealed highly heterogeneous and markedly different patterns in contiguous histological images (Figure 9).

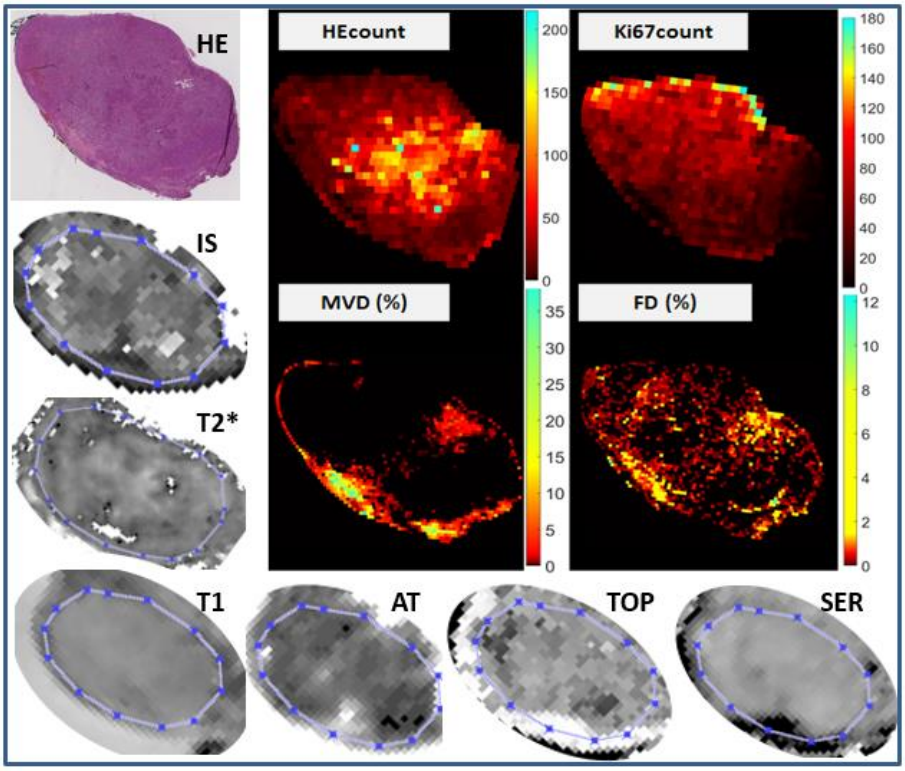

Figure 9. HE section, heat maps and selected MR parameter maps from one of the studied GOT1 tumours that responded to therapy by markedly reduced tumour volume (marked with #3 in Figure 2). Delineations on MR parameter maps show tumour boundaries. Note the difference in tumour shape between histological sections/heat maps and *e.g. T1* map. A typical landmark for registration is visible in the lower left part of the tumour which, *e.g.*, show low intensity on *IS* and *SER* maps, but high intensity on MVD heat map

Correlations between MR parameters and histological indices (III)

The results from the linear mixed-effects regression analysis are summarized in Figure 10. Based on statistical significance, HEcount could be predicted by three DCE-MRI parameters (*TOP*, *TTP* and *BE*), Ki67count could be predicted by one DCE-MRI and one relaxation parameter (*IS* and *T1*), as could MVD (*SEmax* and *T1*) and FD could be predicted by one IVIM-DWI parameter (*f*). Other strong correlations that almost reached statistical significance were also found, *e.g.* between HEcount and *SER* or MVD and *AUCn*.

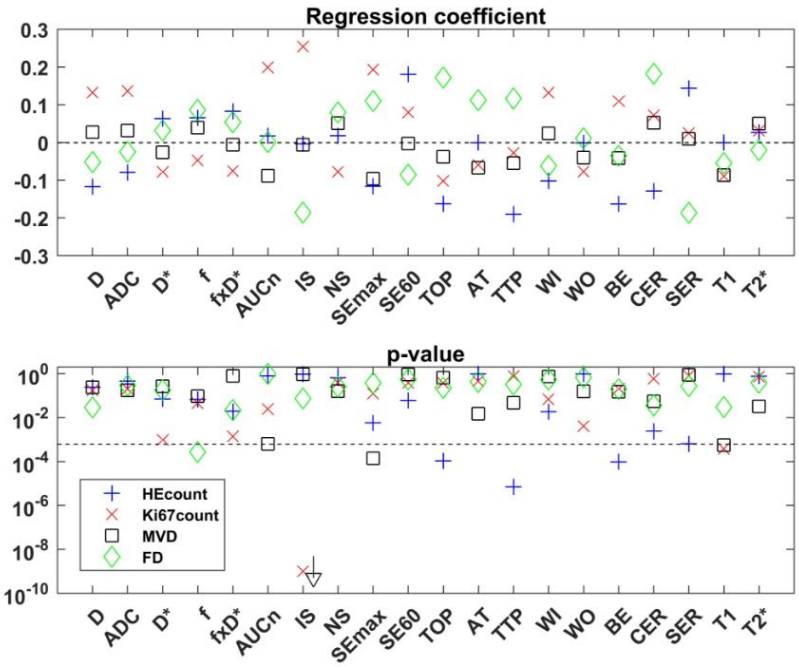

Figure 10. Regression coefficients (upper plot) with corresponding p-values (lower plot) for pairwise associations of MR parameters and histological indices found in **III**. The correlations are based on 1821 samples from the five tumours, where each sample contain four histological indices and 20 MR parameters extracted from a 250x250 μm^2 tumour region. Linear mixed-effects regression was used to account for random effects by *e.g*. coil setup, tissue preparation or colour threshold levels. A vertical dashed line in the lower plot shows the p = 0.05 level adjusted for multiple comparisons. The p-value for IS vs. Ki67count was 1.5e-23 (adapted from **III**)

Uniqueness of MR parameter information (III)

The dendogram of the cluster analysis of MR parameters is shown in Figure 11. It demonstrates similarities between *CER* and *SEmax*, which was expected due to their similar definitions. Another expected similarity was found between *D* and *ADC*, as well as between *D** and *D*xf*. Viewed from a perspective of differences (from above in Figure 11), some parameters were regarded more different from others regarding information content, like the single parameters *WO*, *NS*, *T1* and *T2**. Others formed groups of mutual information content, but with little in common with other parameters, such as the perfusion related IVIM-DWI parameters (*f*, *D** and *fxD**) and the diffusion parameters (*D* and *ADC*). One group was formed with many DCE-MRI parameters.

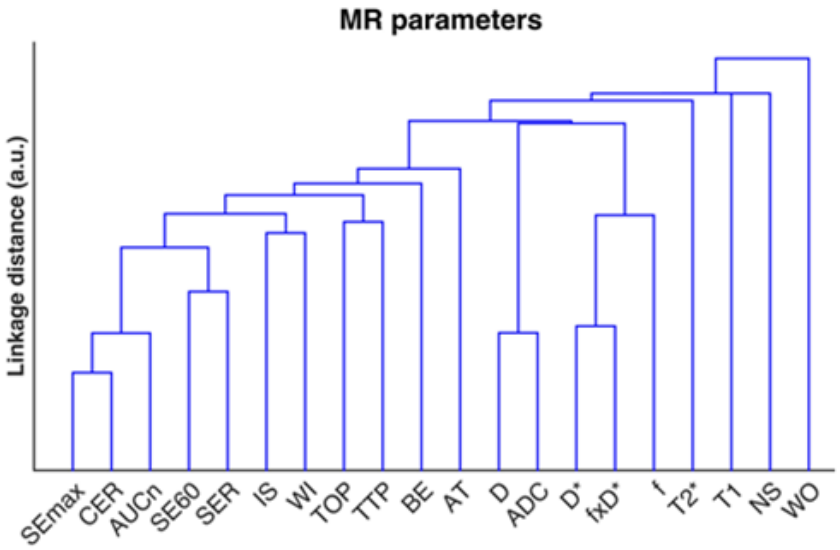

Figure 11. The results of the cluster analysis of the MR parameters is shown in the dendogram. The single linkage distance measure is used. Adapted from **III**

Spatiotemporal MR analysis predicts therapy response (IV)

T2 weighted anatomical imaging of tumour response (IV)

T2 weighted images of two tumours, acquired before and repeatedly after therapy, are shown in Figure 12. The images demonstrate the excellent tumour-to-background tissue contrast that is achievable using T2 weighted imaging. However, although the tumours responded very differently to therapy, neither the heterogeneous tumour patterns, nor the way the patterns change over time reveal any obvious differences between the tumours by visual inspection.

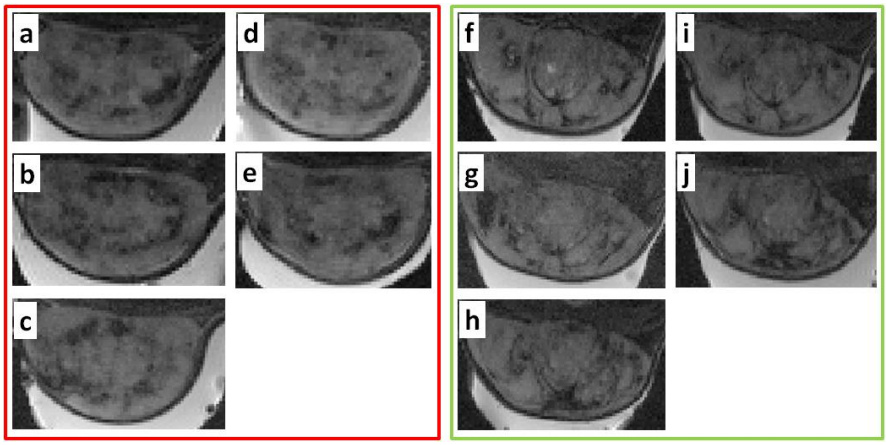

Figure 12. T2 weighted images of a central tumour section in two of the animals in **IV**. The fluctuating dark and bright intra-tumour regions are manifestations of tumour heterogeneity. The gel used for improved field homogeneity is visible as bright regions under the tumours. Left images, framed in red, shows a tumour that continued to grow after treatment. On day -1(a), the tumour volume was estimated to 241 mm^3 (100 %). On days 1 (b), 3 (c), 8 (d) and 13 (e), it reached 104, 109, 136 and 173 %, respectively. The tumour to the right, framed in green, was initially 611 mm^3 (100 %), but after treatment it decreased to 96, 91, 73 and 81 %, on days 1 (g), 3 (h), 8 (i) and 13 (j), respectively. The heterogeneous patterns of the tumours on day -1 are only slightly altered over time, and reveal no obvious differences that can be used to separate the differently responding tumours. This illustrates the necessity of acquiring additional MR parameters for evaluation of biological response to therapy. Note that the sizes of the tumour images were rescaled for better visualization

Correlation between MR features and response (IV)

Many MR features showed significant correlation with response, and each individual correlation is shown in Figure 4 in **IV**. In general, apart from an occasional change of sign, the definition of change of a parameter value over time as absolute or relative had little effect on correlation coefficients (<0.1, data not shown). Some correlations, however, (*e.g.* for *SER* features) were more affected and showed substantially different correlation coefficients depending on definition.

Highly efficacious MR features found in regional and early evaluation (IV)

The MR features reaching a relative cumulated lasso regression coefficient (β-sum) over 0.05 are shown in Figure 13 (the 0.05 display limit was arbitrarily chosen for improved visualization). The feature reaching highest β-sum was *SER* measured peripherally (disc 4) on day -1, with approximately twice the β-sum of the second most important feature, which was the relative increase in *D* in the same disc on Δday -1:3. Five of the MR parameters represented in Figure 13 required disc separation in order to reach the display limit (*e.g. IS*), whereas tumour median sufficed for display of the other 7 MR parameters. Interestingly, a lot of information regarding therapy response seems to be available very early after treatment, since a total of 24 features, based on 10 MR parameters, were displayed on Δday -1:1. The pre-treatment tumour volume was strongly correlated with the response variable (correlation coefficient = -0.60), suggesting that treatment effect improved with tumour volume. Surprisingly, however, it did not reach display limit in Figure 13.

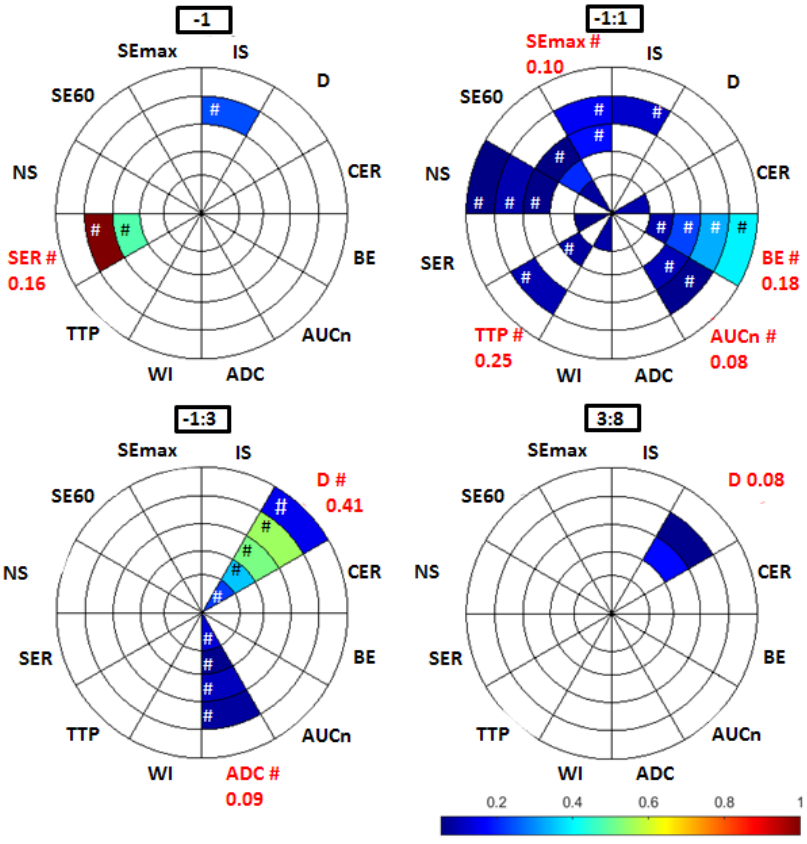

Figure 13. The relative magnitude of the cumulated lasso regression coefficients over 5000 imputations, the β-sums, for individual MR features is indicated by colour, with disc number and MR parameter indicated by the sections of the pie chart. Hash-tag (#) indicates that the feature was based on relative change (*cf.* fig. 12 for sign of correlation). Note that the change in *SE60* between day -1 and 1 (-1:1) in disc 3 differs from disc 1 and 2 regarding definition of change. For clarity of display, features with relative β-sum < 0.05 are not displayed. Adapted from **IV**

Spatiotemporal evaluation of selected MR parameters

The development over time for MR parameter values in different tumour regions (disc 1-5) often differed profoundly between tumours that showed a decreasing volume during the first week after treatment (positive response variable, *cf.* arrows in Figure 2), and tumours that only showed a reduced growth rate (negative response variable). These two groups will henceforth be referred to as shrinking and stabilising, respectively, and some interesting examples are shown in Figures 14-16.

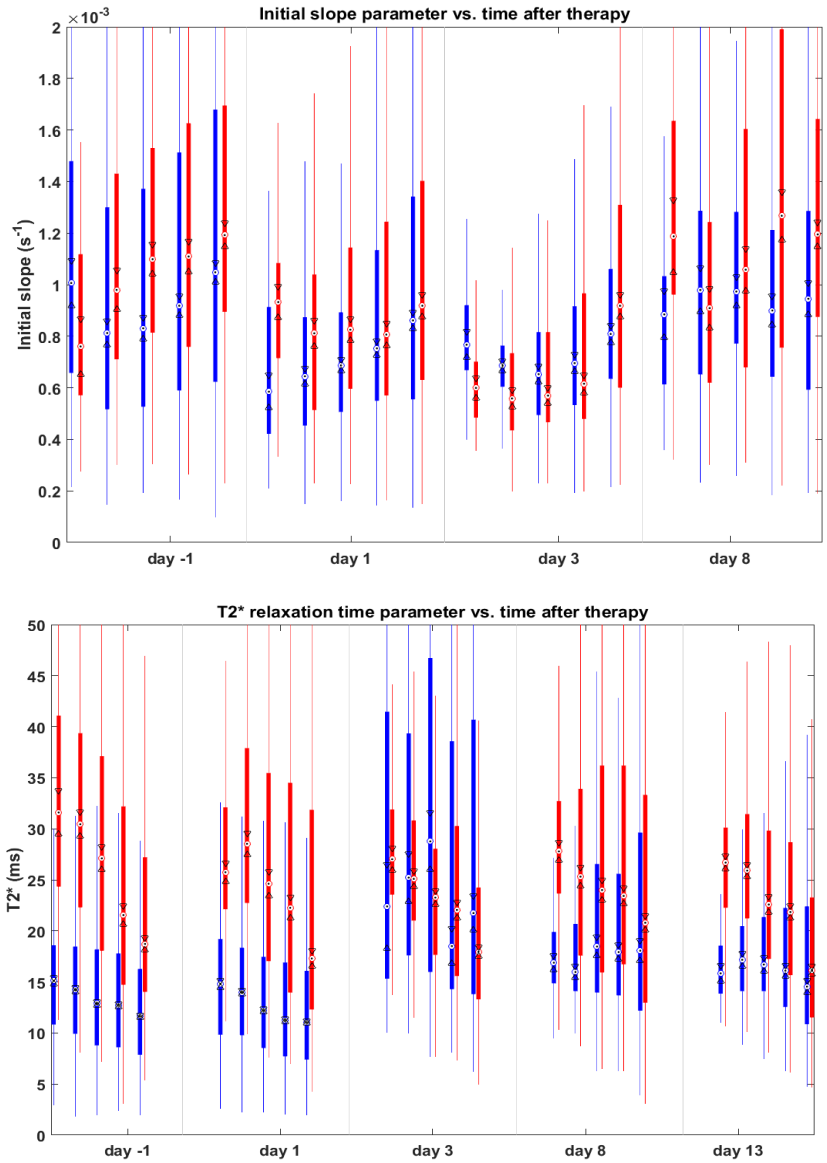

Figure 14. Development of *IS* (upper) and *T2** (lower) in the five discs over time for shrinking (blue) and stabilising (red) tumours. For each day, central tumour values (disc 1) are displayed to the left, and disc numbers are increasing to the right. The median, 25th and 75th percentiles are represented by the middle point, lower and upper bold lines, respectively. Some extreme values and outliers have been left out for display purposes. Two medians are significantly different at the 5% significance level if the intervals marked by the triangular marker do not overlap

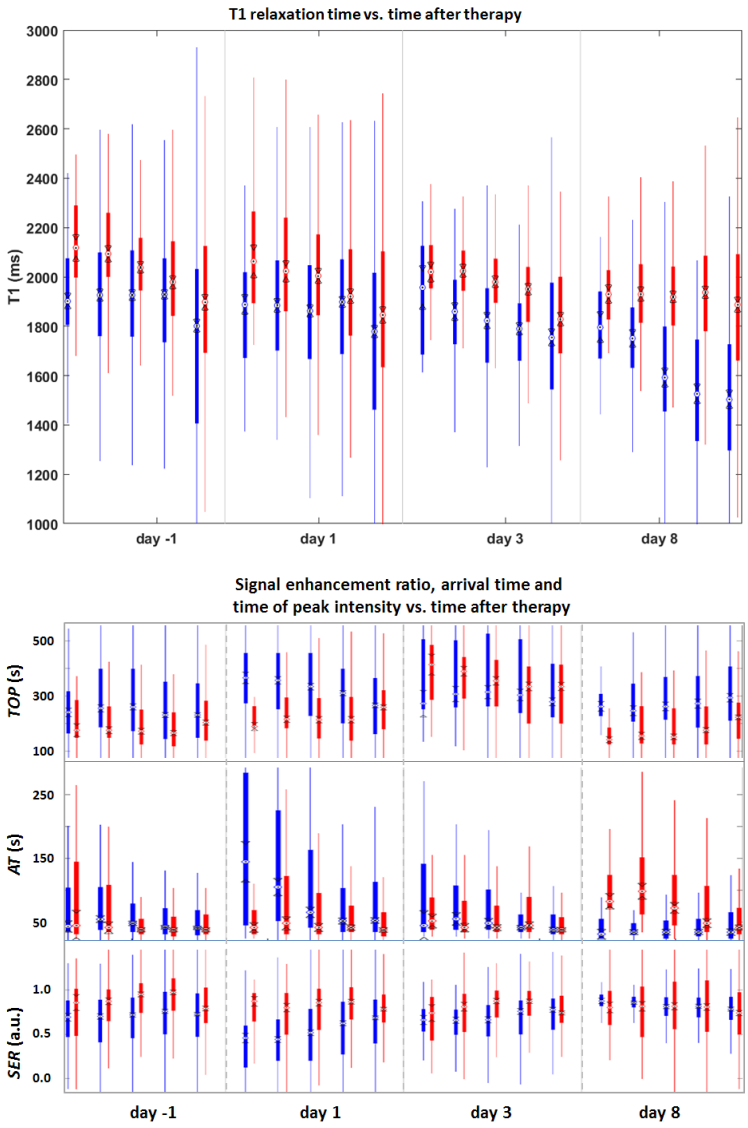

Figure 15. Development of T1 (upper) and *SER*, *AT* and *TOP* (lower) in the five discs over time for shrinking (blue) and stabilising (red) tumours. For each day, central tumour values (disc 1) are displayed to the left, and disc numbers are increasing to the right. The median, 25th and 75th percentiles are represented by the middle point, lower and upper bold lines, respectively. Some extreme values and outliers have been left out for display purposes. Two medians are significantly different at the 5% significance level if the intervals marked by the triangular marker do not overlap

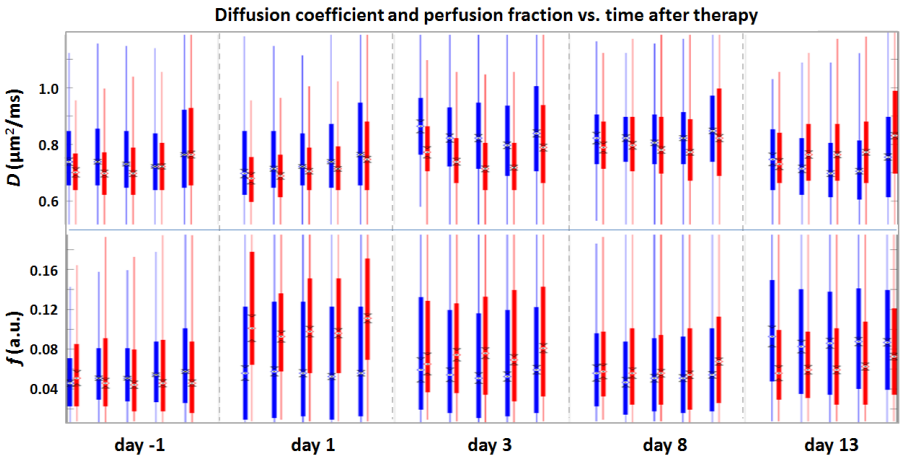

Figure 16. Development of *D* and *f* in the five discs over time for shrinking (blue) and stabilising (red) tumours. For each day, central tumour values (disc 1) are displayed to the left, and disc numbers are increasing to the right. The median, 25th and 75th percentiles are represented by the middle point, lower and upper bold lines, respectively. Some extreme values and outliers have been left out for display purposes. Two medians are significantly different at the 5% significance level if the intervals marked by the triangular marker do not overlap

Biology supports MR findings (IV)

The LC-MS analysis yielded expression ratios for 5381 different proteins, whereof 104 correlated strongly with the response ($p < 0.01$) and were further evaluated. 68, 28 and 8 of the proteins were found in central only, peripheral only and both central and peripheral tumour samples, respectively. Sixty-six of the proteins could be found in different categories of biological processes that are related to response to radiation according to the Gene Ontology database. The protein from each category that was most strongly correlated with response was further evaluated, and of these, two proteins were strongly correlated strongly also with MR features of high importance (high β-sums), namely CATA (Catalase, encoded by *CAT*) and CCD89 (Coiled-Coil Domain Containing 89, encoded by *CCDC89*).

The pre-treatment *SER* in disc 4 (highest β-sum feature) and centrally sampled CCD89 were highly correlated (correlation coefficient (r) = -0.9 and p-value corrected for multiple comparisons (p_c) = 0.03) CCD89 is a protein associated with DNA damage & repair, proliferation, and cell cycle arrest. The relative increase in *D* in disc 4 on Δday -1:3 (2nd highest β-sum feature) and peripherally sampled CATA, a protein associated with oxidative stress, proliferation, cell cycle arrest, and apoptotic cell death, were also

significantly correlated ($r = -0.86$, $p_c = 0.03$*). Additional correlations that did not quite reach statistical significance are listed in **IV.** Interestingly, the tumour volume prior to therapy, which was strongly associated with response, did not correlate significantly with any of the MR features or proteins evaluated.

"It is not the strongest of the species that survive,
nor the most intelligent, but the one most responsive to change."

Charles Darwin

Discussion

Tumour volume for response verification

A decreased viable tumour mass may indicate that the tumour responds to therapy. However, as discussed in **I**, the use of the size of the tumour mass as a measure of therapeutic effect is not unproblematic. The clinical tumour size assessment methods typically rely on measurements of tumour diameters, either externally on palpable tumours, or on *e.g*. images from CT or MRI [66]. This rough estimate of viable tumour volume is problematic for non-spherical or irregular tumours, as well as for disseminated disease with many tumours. Apart from this, a changing tumour size from diagnosis to evaluation of therapy effect is really only indicative of disease progression if the doubling time of the tumour is known [67, 68]. In this thesis, however, the main interest was not long-term effects, but rather the immediate radiobiological effects on tumour tissue, and the associations to MR derived parameters. Therefore, repeated, short-interval tumour volume estimation is probably a reasonable surrogate marker of tumour response. It should also be noted that the purpose of the treatments in the studies was only to induce a suboptimal therapeutic effect, to enable further measurements on the tumours and to correlate MR data with different levels of therapeutic effects expected from heterogeneous responses.

Assuming that MR based tumour volume estimations would provide a more sensitive and accurate response verification method compared with external measurements of tumours dimensions using *e.g*. gauge block, we studied the performance of such methods relative to the golden standard *ex vivo* determination of tumour volumes. The T2 weighted RARE sequence was used to acquire tumour images since the use of 180° refocusing pulses makes it robust to geometrical distortions. However, the accuracy regarding volume assessments still warranted investigation since it could be affected by pixel smoothing effects due to turbo factors and partial volume effects from insufficient voxel sizes in 3D acquisitions, in addition to slice profiles in 2D acquisitions.

Acquisition time is often limited both in the clinical and pre-clinical situation, especially when additional experiments are to be conducted within the same imaging session. This makes 2D sequences suitable since they require only a fraction of the time required by 3D acquisitions, especially for large tumours requiring large matrix sizes. We found that 2D acquisitions were adequate to produce high correlations with resected tumour volumes, but that the interobserver variability increased when tumours were very small. This was probably due to partial volume effects. One remedy would

thus be to decrease slice thickness if allowed by the slice selection gradient performance and SNR. However, these considerations are only necessary if the range of tumour volumes in a particular study includes both very small and very large tumours. If all tumours are really small, 3D methods should be preferred. T1 weighted acquisitions are generally faster than T2 weighted acquisitions, but often require contrast injections for proper visualization of tumours.

Other imaging modalities can be used for non-invasive tumour imaging, but requirements on spatial resolution makes some more interesting for tumour volume measurements, such as micro-CT for small animal studies. Micro-CT has shown excellent results regarding tumour volume assessment, with only a few minutes of acquisition time [69]. However, CT does not offer the same versatility as MR regarding tumour applications, and it often requires contrast injections. The ionizing radiation used by CT inevitably results in an absorbed dose to the tumour, typically 0.1-0.3 Gy per examination, which may confound results in therapy response assessments [70, 71].

The 2D acquisition method discussed above was chosen for tumour volume assessment in **IV**. The tumours volumes determined for the 21 included animals were in general larger than 200 mm^3 (0.2 g) (median estimated tumour volume day -1: 460 mm^3, range: 137 to 689 mm^3) throughout the study, and it is therefore likely that the actual tumour volumes were of adequate size for the 2D method (*cf.* **I**). Only 3/21 tumours were smaller than 200 mm^3 on the day -1 measurement, and only 2 tumours reached a volume < 100 mm^3 after treatment. The absolute changes in volume between days were, however, often smaller than 200 mm^3, but errors in the response variable imposed by partial volume effects should be low since response was defined by the regression coefficient of several measurements, which should have an averaging effect on the estimates.

Model parameter optimization

Some MR parameters included in this thesis were estimated using models of the MR signal behaviour under different conditions. The IVIM model describes the diffusion weighted MR signal behaviour for different levels of diffusion weighting, and it differs from the other applied models due to the compartmentalization of different diffusion phenomena, which makes it bi-exponential [35]. A minimum of three model parameters (*D, f* and *D**) needs to be estimated. We investigated several methods to achieve proper quality of the estimates, including fitting of all three parameters simultaneously using non-linear least squares methods, stepwise fitting of *D* using a simple mono-exponential model, followed by fitting *f* and *D** using the first method with *D* fixed, and we also investigated the Bayesian approach described in **II**

(data only shown for the Bayesian approach). The latter was superior regarding the quality of *f* and *D** in most situations.

At the SNR levels achievable in diffusion weighted imaging, where MR signal is intentionally destroyed by the diffusion gradients, the choice of prior distribution in particular, but also of central tendency representation, becomes very important for Bayesian model fitting. This was confirmed by the results of this study, where the choice of prior distribution was found to have a significant impact. The uniform prior resulted in more stable parameter estimates in both simulations and *in vivo* experiments. The choice of central tendency representation was less important for estimating *D* and *f*, whereas mode representation seemed to be required for *D** parameter estimates with acceptable errors. The results of this study emphasise the importance of reporting not only acquisition parameters such as the *b*-values, but also which methods were used for model fitting in IVIM-DWI studies, since this should be taken into account when comparing results from different studies.

MR methods for response assessment

The remainder of this discussion will mainly focus on MR parameters that were found interesting in **III** and **IV**, and highlight those that seem promising as surrogate biomarkers for biological processes of importance for ^{177}Lu-octreotate therapy on small intestine NETs.

The association between MR parameters and biological tumour features represented by histological findings were evaluated in **III** (Figure 10). In general, the MR parameters that were significantly correlated with HEcount and Ki67count were those reflecting rates of contrast agent delivery to tissue and exchange rates between tissue and vasculature, *i.e*. parameters describing perfusion, and higher perfusion was related to increased HEcount and KI67count. Interestingly, the perfusion fraction (*f*) was positively correlated with FD, and negative correlations were found between MVD and MR parameters reflecting the amount of contrast agent reaching the tissue.

We expected to find correlations between diffusion parameters *D* or *ADC* and histological parameters reflecting parameters that affect cell density, but we did not. When data was re-evaluated with information from **IV**, however, it became clear that the diffusion was only transiently increased on day 3, whereas correlations with histology were evaluated from measurements on day 1 and 13. A temporal mismatch between the condensation of chromatin measured on histology and subsequently increased diffusion due to reduced cell density, measured with DWI-MRI, may thus confound these types of correlations.

On a statistically significant level, three DCE-MRI parameters (*TOP*, *TTP* and *BE*) were able to predict HEcount, one (*SEmax*) was able to predict MVD and one (*IS*) was able to predict Ki67count. In DCE-MRI, a contrast agent is i.v. injected during acquisition, and the increased signal intensity in an image pixel is assumed to be proportional to the contrast agent concentration in the EES [72, 73]. By analysing the signal time-intensity curve (TIC), information on micro-vascular structure and functionality, as well as tissue characteristics that affect the delivery of therapeutic agents to the tumour cells can be acquired from each pixel. The vascular density sets an upper limit for the amount of oxygen, nutrients and pharmaceuticals that reach the tissue, and thereby the cells of a tumour, but the functional properties of the vessels may be of even more importance for successful delivery [50, 74-76]. For example, studies on both prostate and pancreatic tumour models showed that the uptake of radiolabelled tracers correlated with functional DCE-MRI parameters that reflect perfusion and trans-endothelial transport (*e.g. TTP*, *IS*, *SE60*, *WI* and *WO*), whereas weaker correlations were found for contrast agent amount-related parameters (*e.g. AUCn*, *CER* and *SEmax*) [50, 76]. This is a possible explanation to the apparent mismatch between MVD and Ki67count observed in the heat maps in Figure 9. Proliferative activity requires supply of nutrients and oxygen and thereby vasculature, but MVD may be more related to angiogenesis and VEGF expression in tumours, than to the actual perfusion [74, 77, 78]. Histologic staining for vascular functionality, such as the combined staining for endothelial cells and pericytes, the latter required for proper vascular function, may better match information on proliferation [78].

A statistically significant and positive correlation was found between initial slope (*IS)* and Ki67count ($p = 1.5x10^{-23}$) (**III**). *IS* mostly describe the initial phase of the TIC, and is a functional measure that relies on the blood perfusion, the extravasation of contrast agent from the vascular lumen to the EES and, to some extent, the volume of the EES [73, 79]. The extravasation rate depends on the micro-vessel permeability and surface area, but the angiogenic and immature vasculature of tumours makes permeability abnormally high, and combined with the low molecular weight of the contrast agent, *IS* is more likely to reflect perfusion than vessel permeability and surface area [25, 73, 80]. It seems reasonable that the most proliferative, or viable, tumour cells were found in regions of adequate perfusion, since they would require efficient delivery of oxygen and nutrients. It is thus possible that low *IS* indicates hypoxia. We did not perform histological staining for hypoxia, but it has been associated with long *TTP* and *TOP* in prostate cancer in rats, whereas normoxic regions showed short *TTP* and *TOP* Cho, Ackerstaff [51]. Long *TTP* and *TOP* should correspond to low *IS.*

In fact, *IS* and *TOP* demonstrated a statistically significant and strong negative correlation in our data (not shown).

Based on our data, the feature selection method regarded *IS* important for response assessment (**IV**), particularly in peripheral tumour (disc 4) and for very early assessment (Δday -1:1) or prediction of response (day -1) (Figure 13). Tumours with lower *IS* values in disc 4 prior to therapy responded with decreasing volume, whereas those with higher values only stabilised. Enhancement in peripheral tumour only has been correlated with reduced tumour response after radiotherapy in cervical cancer patients, whereas homogeneous enhancement indicated better response. On histological evaluation, increased permeability and abundant cancer cells were found in responding tumours, as opposed to increased fibrosis in non-enhancing regions of non-responding tumours [81, 82]. In our study, the shrinking tumours had similar *IS* in central and peripheral tumour on day -1, whereas stabilising tumours had significantly lower central *IS* (Figure 14). Adequate perfusion throughout the tumour may have provided access to the therapeutic agent, which may explain the volume reduction. However, it does not explain the lack of volume reduction in stabilising tumours, which seem to have higher *IS* in most parts of the tumours. It thus seems like tumours that were only stabilised were somehow more radioresistant.

Several other highly interesting differences were found between the shrinking and stabilising tumours prior to therapy, which may offer explanations to the different response and/or provide potential biomarkers for tumour response. For example, compared with shrinking tumours, the stabilising tumours had a markedly higher *T2**, shorter *TOP* and higher *SER* throughout the tumour, and a lower *D* but higher *T1* in central tumour (Figures 14-16). Interestingly, there was also a positive correlation between tumour size before treatment and response (**IV**), meaning that larger tumours showed greater relative volume reduction after therapy. One hypothesis is that stabilising, *i.e*. smaller tumours receive less absorbed tumour dose, since the dimensions of the tumour is more comparable with the range of the emitted beta particles.

*T2** is sensitive to the presence of paramagnetic deoxyhaemoglobin due to dephasing of transversal magnetization, and T2* has been positively correlated with partial oxygen pressure (pO_2) in tumour tissue [83, 84]. This would imply that the pO_2 was lower in the shrinking tumours than in the stabilising tumours prior to therapy (Figure 14), which contradicts the fact that radiotherapy is more effective in well oxygenated tumours. However, if a higher number of tumour cells are viable and proliferating, it is possible that the generally high consumption of oxygen is causing the increased

deoxyhaemoglobin levels in the shrinking tumours, resulting in reduced T2*. The immature and chaotic vasculature of tumours may not be able to sustain pO_2 levels, or reduce deoxyhaemoglobin levels, under such highly oxygen demanding conditions, but there may still be sufficient amount of oxygen for cell viability and adequate response [85]. Rodrigues *et al*. [86] investigated the association between pre-treatment R2* (=1/T2*) and response to radiotherapy in a rat prolactinoma and a mouse fibrosarcoma tumour model. They found that the model with lowest pre-treatment T2* (prolactinoma) responded with tumour volume reduction, whereas the other tumours did not. Furthermore, among the individual prolactinomas, there was a linear relation between pre-treatment R2* and volume reduction. These results are thus in agreement with our results, even though they used a different tumour model, and that there were some other discrepancies between the studies. They used x-rays and were thus independent of adequate delivery of the pharmaceutical, a higher absorbed tumour dose (15 Gy) and a 4.7 T MR system, which may influence susceptibility effects of the deoxyhaemoglobin.

Lower T2* has also been associated with lower blood flow and blood volume, and regions with reduced oxygenation are often characterized by reduced vascularization and delayed and persisting signal enhancement [51, 87]. It is thus possible that the shrinking tumours are homogeneously, but less supplied with blood flow, although adequate for sustained proliferation. This is supported by the fact that *IS* was lower in the greater part of shrinking tumours, but also by the higher *TOP* (delayed enhancement) and lower *SER* (relatively high late enhancement) in these tumours (Figure 15). As opposed to normal tissues, blood flow and glucose metabolism of tumours are not necessarily linearly correlated. For example, a high metabolism to blood flow ratio was observed in locally advanced breast cancer patients prior to chemotherapy, as measured by ^{18}F-FDG and ^{15}O-water PET, respectively. The ratio was reduced to close to normal tissue ratios in patients responding with reduced tumour burden whereas blood flow was less affected, suggesting a reduced number of metabolically active tumour cells [88]. This would explain the sudden, significant increase in T2* in the shrinking group on day 3 of our study (**IV**), since decreased metabolism due to fewer viable cells would produce less deoxyhaemoglobin. Our results also indicate early reduced blood flow, based on the generally decreasing *IS* and increasing *AT* and *TOP* on day 1 and 3 (Figures 14-15).

The pre-treatment signal enhancement ratio (*SER*) in rather peripheral tumour (disc 4 in particular) was found to be very important for tumour response to ^{177}Lu-octreotate therapy (**IV**). It was negatively correlated with HEcount and almost reached statistical significance (**IV**). *SER* decreased significantly in most parts of the shrinking tumours (disc 1-4), but only in

disc 3-4 in stabilising tumours. *SER* is the ratio of early to late relative signal enhancement, and it has been closely correlated with the better understood pharmacokinetic redistribution rate constant *k*ep, which in turn has been correlated with histologic grade and prognosis in breast cancer [89-91]. In patients undergoing neoadjuvant chemotherapy for locally advanced breast cancer, *SER* correlated positively with changes in glucose delivery to tumour tissue, as estimated by ^{18}F-FDG [92]. Others have verified that decreased *SER* correlates with decreased glucose delivery by ^{18}F-FDG PET, and decreased blood flow by ^{15}O-water PET, but no significant correlation was found between SER and glucose metabolism [93].

A decreased *SER* thus indicates increased apoptosis, which seems reasonable in the shrinking tumours (Figure 15), and it is supported by a previous study on the same tumour model, where apoptosis was significantly increased day 1 and 3 after treatment using 30 MBq ^{177}Lu-octreotate [94]. On days 7 and 13, the apoptotic count was lower, as well as the number of tumour cells.

It thus seems like *SER* is another promising biomarker for perfusion effects in NETs, with possible applications also in imaging of apoptosis, and since its definition is based on the relative enhancement at two distinct time points, it may provide information that is not provided by *IS* and *vice versa*. SER may be advantageous to *k*ep since it does not require time consuming T1 mapping, nor does it require estimation or measurement of the arterial input function.

The longitudinal relaxation time constant *T1* showed modest but statistically significant, negative correlations with MVD and Ki67count (Figure 10) (**III**). Although the feature selection method did not regard it as one of the most important parameters to monitor for this combination of tumour model and therapy method (**IV**), there was a clear separation between tumour shrinking and tumours only stabilising. Tumours shrinking had lower T1 on all days and discs, there was a pronounced, almost linearly increasing *T1* from peripheral to central tumour in stabilising tumours, and on day 8, this *T1* gradient was reduced, and shrinking tumour T1 was decreased (Figure 15).

T1 is sensitive to the molecular microenvironment of the water protons, in particular macromolecular concentration. In tumours, vessel permeability allows plasma proteins to leak to the EES where they are retained due to limited lymphatic drainage, and *T1* is thus reduced. Treatments inhibiting angiogenesis, and thereby decreasing MVD, have resulted in increased tumour *T1* [55, 56]. This may be due to the reduced number of macromolecules that were previously involved in vascular remodelling,

growth factor signalling etc., but also due to typically reduced vascular permeability, or vascular normalisation, that hinder protein leakage [77].

On a mouse model of ovarian adenocarcinoma, anti-angiogenic therapy increased *T1* but decreased micro-vessel density and proliferation (determined from CD31 and Ki67 staining) [55]. These results support our findings regarding the association between *T1*, MVD and Ki67count, but we did not observe an increased T1 after therapy (Figure 15). Instead, *T1* was rather unchanged between day -1 and 3, before the change on day 8 mentioned above. However, we used a completely different treatment modality that is not directly targeting the vasculature, and there may be less vascular normalisation after radionuclide therapy. The lower *T1* in shrinking tumours may indicate a higher proliferative (Ki67count) and apoptotic (HEcount) activity, with a high rate of tissue degradation and biosynthesis, which should result in high tissue concentrations of macromolecules. The regrowth of these tumours seen after day 8 (**IV**) and the sudden drop in *T1* (Figure 15), may thus indicate increased proliferation.

An interesting observation is that before treatment the tumours that only stabilise in volume show an almost linear radial gradient in several MR parameters; with increasing radius *IS* increase, *T1* decrease and *T2** decrease (Figures 14-15). This effect was not observed in the shrinking tumours, except for a minor decrease in *T2**. The finding suggests that there is increasing perfusion, concentration of macromolecules and deoxyhaemoglobin from central to peripheral tumour regions in the stabilising tumours. The histological associations (Figure 10) further suggest that proliferation and MVD are higher in the peripheral regions of these tumours. Radial differences in tumour characteristics have been observed in both animals and patients with different tumour types, probably partly caused by increased tumour IFP, which in turn is associated with increased malignancy, hypoxia and metastases [6, 10, 12, 52, 95, 96]. For example, in two types of human melanoma xenografts (R-18 and T-22) there were significantly higher degrees of hypoxia in central tumour and MVD in peripheral tumour, and both parameters were positively correlated with central IFP for IFP > 20 mmHg [52]. Gilliksrud *et al.* [95] investigated human melanoma xenografts in mice and found that a DCE-MRI parameter similar to the volume transfer constant of contrast agent (*K*trans) was highest in peripheral tumour and lowest in central tumour, and that it was negatively correlated with IFP. The same correlation has been found in cervical cancer in patients, but without reference to tumour regions [96]. With abnormal and leaky microvasculature in combination with inadequate lymphatic drainage, the IFP eventually rises to levels comparable with the intravascular pressure, which reduce perfusion, or even cause complete flow stasis [77]. Typically,

IFP is increased throughout the tumour, but rapidly decrease at the periphery [10, 97]. Rofstad et *al*. suggested that the pro-angiogenic factors that result from the hypoxia are transported towards the periphery by the interstitial net radial fluid flow caused by the central IFP, and that they promote the excessive peripheral angiogenesis [52].

This offers an explanation, in addition to the tumour size, to the varying therapy response in the different tumours. Some may be of a more aggressive, resistant and angiogenic phenotype than others, and may have developed a higher IFP. A radial fluid flow may result in successively increased concentration of macromolecules and proangiogenic factors (decreasing *T1* and increasing MVD), increased perfusion (*IS*), proliferation (Ki67count) and thereby high oxygen consumption (reduced T2*). It would explain the linear radial gradient of the MR parameters described above. However, the profound T2* gradient (Figure 14) should not be interpreted solely as reflecting a corresponding gradient of deoxyhaemoglobin concentration. Other factors are probably also involved, such as altered metabolism triggered by hypoxia and hemosiderin deposits. Furthermore, T2* is more likely linked to deoxyhaemoglobin levels in acute hypoxia, *i.e*. caused by fluctuating perfusion, and this type of hypoxia may be less pronounced in peripheral tumour [47].

Nevertheless, the combined information provided by the MR parameters that demonstrate these radial gradients makes it reasonable to believe that they do reflect tumour characteristics typically associated with therapy resistance, such as IFP, hypoxia angiogenesis and malignant progression. It also demonstrate the importance of evaluating tumours on a more regional level, such as the discs used by us, instead of reporting an average value of the entire tumour.

Statistically significant associations were found between HEcount and *BE*, *TTP* and *TOP* (Figure 10) (**III**). Apoptosis was more present in regions of short *BE*, *TTP*, *TOP*, and it seems reasonable that increased access to these regions (higher perfusion, or *IS*) to the ^{177}Lu-octreotate resulted in increased apoptosis. We did not, however, find any association between apoptosis and diffusion measured by DWI-MRI. Neither did diffusion parameters correlate with *e.g*. FD, which represents acellular tissue. Possible explanations are unfortunate image registration or cell reorganisation due to chemical water extraction and rehydration during histological preparation. However, based on our data, it seems like diffusion measures are more suited for longitudinal assessments that evaluate changes in parameter values, rather than the actual parameter value. In **IV**, both *D* and *ADC* were regarded very important to monitor, but it was their value relative to the pre-treatment value (on day 3)

that was important. Figure 16 also clearly shows that there was an increased *D* in shrinking tumours on day 3, but also on day 8, most likely due to decreased cell density as expected after being exposed to irradiation [98]. On day 13, *D* was reduced again, which is also expected due to the regrowth observed at that time. The results are in agreement with a previous study on the GOT1 tumour model treated using 30 MBq ^{177}Lu-octreotate. A high number of apoptotic tumour cells were seen on histological evaluation after therapy, with highest counts reached on day 1 and 3 [94]. The *ADC* parameter showed trends similar to *D*, and is therefore not shown. However, the separation between the shrinking and stabilising tumours was not as obvious, which may be related to the fact that ADC is more sensitive to perfusion effects [35].

It should be noted that the value of *BE* in this study may be negatively biased by the relatively short duration of the DCE-MRI experiment imposed by a hardware limitation. The ~5 minutes of TIC monitoring may not be enough to accurately measure the negative slope of the curve that was necessary for *BE* calculation, but it should be adequate for *TTP* or *TOP* measurements.

The perfusion fraction (*f*) showed statistically significant positive correlation with FD, and was thereby the only evaluated MR parameter that was able to predict the presence of fibrotic tissue (**III**). This makes *f* interesting *e.g.* for treatment verification, since fibrosis has been demonstrated in previously apoptotic regions after successful treatment of GOT1 and other tumour models [59, 94, 99].

Furthermore, *f* separated shrinking from stabilising tumours on day 1 by the substantially increased *f* in the latter tumours (Figure 16). If the treatment had an early effect on the vasculature, *e.g.* pruning immature vasculature by killing radiosensitive endothelial cells and thereby normalizing the vasculature, it may have resulted in the increased *f* that was observed, as well as the less radial dependence of *IS* by improved perfusion in central tumour. Interestingly, both the pre-treatment values and the increase in *f* were similar in all discs, whereas *e.g. IS* clearly demonstrated decreasing values toward the tumour centre. This indicates that *IS* and *f* provide independent information on perfusion or pseudo-diffusion effects, which is supported also by the separation in the clustering analysis (Figure 11).

Unfortunately, the *D** estimation most likely failed in many tumours of our experiments, which may have affected also the estimation of *f*, and definitely *fxD**. Nevertheless, the gradual development of *f* over time after day 1 indicates that the effects are not due to *e.g.* failed parameter estimation.

Other factors, such as partial volume effects involving blood flow in larger vessels, may influence *f* in particular, and partly explain the different behaviour of *IS* and *f* [100]. A statistically significant, strong correlation was demonstrated between the product *fxD** and IFP in a mouse mammary carcinoma model. IFP was lower for increased values of *fxD**, and highly different IFP values were observed between tumours, as measured by the reliable but invasive wick-in-needle technique [46]. It is thus motivated with additional efforts to improve estimations of *D**, particularly since it could be combined with *f* to non-invasively measure IFP, which would be of great interest in the clinics due to the many associations between IFP and treatment resistance [46].

The evaluation of the results from quantitative proteomics on central and peripheral tumour samples verified that there are biological differences between central and peripheral tumour, and that these differences may be related to response to radiation (**IV**). This data supports the radial MR parameter gradients discussed above.

Relatively few features based on disc 5 were considered important for response assessment (Figure 13), and several MR parameters that were able to separate shrinking from stabilising tumours seemed to abruptly converge in disc 5 (see *e.g.* T2*, day 8-13). This may be due to PVE, *i.e*. that data from normal tissue confound the disc 5 data, but it could also be an effect of a net transport of biological compounds to these regions. If constituents from the entire tumour accumulate in peripheral tumour, it may have a direct effect on the MR signal, but it may also trigger *e.g*. angiogenesis by accumulation of pro-angiogenic signal molecules, even if it was not biologically required [10, 52]. This may render the interpretation of associations between MR parameters and tumour biology complicated in peripheral tumour.

Other, more obvious limitations in this thesis were mostly related to the difficulties commonly involved in spatial registration between images and *ex vivo* tissue analyses, as discussed in **III-IV**. A higher number of animals included in the analysis would have been preferred, particularly for improved statistics in the correlations between MR parameters and histological indices (**III**). When studies rely on the availability of tumours of a suitable size and radionuclides of finite half-life, as well as the availability to the MR system, there is a natural barrier to high numbers of study subjects. The sensitivity of certain MR sequences to unfavourable scanning conditions, such as inhomogeneous magnetic fields or low SNR, also reduce the number of study subjects that are finally included in the analysis. Still, we believe that the hypothesis seeking nature of studies like the ones

presented in this thesis provide adequate information for decisions on further, more in-depth studies of interesting findings, even if there is too few study subjects to make conclusions on each separate finding of this thesis.

Perhaps more of a confounding effect than a study limitation is the fact that it is difficult monitor which regions of the tumour that account for the actual volume changes. *I.e.* if a tumour shrank due to successful therapy in disc 5, the next measurement will regard another tumour region (most likely previous disc 4) as disc 5. Further development of alternatives to longitudinally monitor specific tumour regions are required to overcome this confounding effect.

Conclusions

Tumour volumes can be determined with high accuracy for very small tumours (0.01-0.1 g). 3D methods are more accurate than 2D methods but are very time consuming, whereas 2D methods still provide high accuracy and require less than 10 minutes of acquisition time, which enables additional imaging experiments within one MR session.

Robust IVIM-MRI parameter estimates can be provided by the Bayesian model fitting algorithm, provided that the uniform prior distribution and the mode representation of the resulting voxel parameter distributions are used. However, the method needs further improvement and optimization in order to provide robust estimations of the pseudo-diffusion coefficient.

There were statistically significant associations between several tissue parameters derived from MR methods and parameters derived from histological representations of the underlying tumour biology. Apoptosis, proliferation, microvascular density and fibrotic density could be predicted by the combined use of parameters derived from DCE-MRI, T1 and T2* quantification and IVIM-DWI.

The multiple MR parameters evaluated demonstrated both longer lasting and transient effects on different occasions after radionuclide therapy. Pronounced radial differences were observed, and they were confirmed by differences in central and peripheral expression levels of proteins involved in radiobiological processes. Spatiotemporally resolved multiparametric MR assessments may provide substantial amounts of information of relevance for response assessment.

Based on the results, several potential imaging biomarkers for tumour therapy response assessment are proposed. DCE-MRI provided parameters that reflect perfusion and proliferative activity in NETs, with possible sensitivity also for tissue oxygenation. DWI-MRI evaluated using the IVIM model indirectly provided information on successful therapy by alterations in molecular diffusion and pseudo-diffusion effects, but timing of measurement was critical. T2* relaxation may provide a biomarker of oxygen consumption by tumour cells and cells in the TME, but requires validation using *e.g.* PET methods. T1 provides information on the TME regarding macromolecular content, and possibly also on the interstitial pressure.

"Only those who will risk going too far
can possibly find out how far one can go."

T. S. Eliot

Future aspects

This thesis describes four distinct projects with the common aim of investigating and developing a multiparametric MR approach to predict and assess the response of neuroendocrine tumours subjected to radionuclide therapy. Several aspects of future consideration were unravelled during the work.

For further understanding of the associations between MR parameters and tumour biology, additional methods and histological stains need to be studied, and they should provide information on, *e.g.*, IFP, angiogenesis, oxygenation, acidosis, inflammatory status and metabolism. Preferably, such methods should also be non-invasive and provide spatial information, which would also require additional research and development. In addition to increased understanding of the biological mechanisms behind MR parameters, methods to non-invasively estimate *e.g.* IFP, angiogenesis and hypoxia would be of great value with immediate clinical implications, such as prognosis and treatment decision making. Other imaging methods, such as PET, should complement MR studies on tumours. In particular, studies combining *T2**, *SER* and *IS* with ^{18}F-FDG and ^{15}O-water PET would be highly interesting and may provide additional understanding of the MR parameters related to metabolism and diffusion/perfusion. For improved understanding of parameters, regardless of method, measurements should be made also prior to therapy in order to have better a priori knowledge of their behaviour in the non-treated tumour.

It is also of utmost importance to continue the development of acquisition and post-processing techniques of all MR methods included. IVIM-MRI may require extra attention before it can provide robust estimations regarding pseudo-diffusion effects, and optimization needs to address choice of b-values, diffusion gradient timing parameters, model selection parameters and fitting procedures. However, the biophysical specificity must be balanced by the clinical feasibility, which makes it important to optimise the imaging protocol, both regarding acquisition time and quality of parameter estimates.

Contrast agents with higher molecular weights show less extravasation into EES in tumours, and have shown promise to provide information on tumour IFP. Such agents should therefore be evaluated for additional DCE-MRI experiments.

MR spectroscopy is another highly interesting candidate that should be included in the multiparametric MR methods, since it provides information on the metabolism of the tumour. *Ex vivo* high resolution magic angle

spinning MR spectroscopy should be included as a method to verify the *in vivo* findings and to provide additional, more detailed information on the tumour metabolism. Imaging of the tumour metabolism has also been enabled by the advent of dynamic nuclear polarization techniques, which allows *in vivo* hyperpolarized ^{13}C MRI of tumours. This technique has the advantage over ^{18}F-FDG PET in that is does not rely on ionizing radiation, and the spatial resolution is superior. It allows, *e.g.*, imaging of treatment induced cell death due to the reduced flux of ^{13}C label from pyruvate to lactate, and initial studies on patients with prostate cancer seem very promising. An interesting alternative to, or combination with, hyperpolarized ^{13}C MRI would be chemical exchange saturation transfer (CEST) MRI, which may allow imaging of *e.g.* intracellular pH or glucose accumulation.

One great obstacle to overcome in the development of MR imaging biomarkers for tumour characteristics is to ensure proper spatial registration between the image voxel and the corresponding tissue voxel. Several issues need to be resolved before proper registration is practically achievable, particularly regarding the amount of work and time required per animal. If invasive procedures are required to map also, *e.g.*, IFP, an additional dimension of the registration procedure must be accommodated. Of particular interest would be means to introduce fiducial markers into the tissue non-invasively, which were discernible both on MR images and histological sections, but with minimal toxic effects or local inflammation. Promising approaches are inert polystyrene microspheres containing iron oxide and fluorescent dye, or acrylic paints, such as iridescent stainless steel or bronze paint. Dot-shaped landmarks based on minimal injections of such substances are visible on MRI and histology, and follow tissue shrinkage or movements through histological fixation and dehydration processes. By injection during needle extraction, it is possible to create line-shaped landmarks as well, which could be used to create 3D reconstructions of histological sections, which allows subsequent registration of MR- and histological volumes. The influence of such, rather invasive, methods on the tumour biology under study would, however, require careful evaluation.

Better knowledge on the radiobiological effects on tissue from ^{177}Lu-ocreotate therapy is required to better understand the effects observed with MR methods after treatment. How does *e.g.* heterogeneous absorbed dose distribution affect the response in different parts of the tumour? Furthermore, the dose-response relationship must be studied. Different amounts of activity of ^{177}Lu-ocreotate must be studied in order to evaluate the MR parameters in the entire range of tissue manifestations, from complete response to no response at all, as expected after different dose levels, and improved understanding of when relevant response mechanisms

take place would provide better understanding of the dynamic behaviour of each MR parameter after therapy.

In this work, quantitative proteomics was used to demonstrate biological differences in central and peripheral tumour. Future techniques to collect tissue for *ex vivo* analysis need to allow objective tissue sampling with refined spatial information that better match the spatial resolution of the tumour sub-regions being analysed, such as the discs in this work. Biological verification is important before multiparametric MR based biomarkers can be of clinical value.

In this thesis, the potential of evaluating response locally in tumour sub-regions, such as the discs, was demonstrated, and when MR methods and spatial registration procedures are improved, further refinement of the tumour separation into smaller regions should be evaluated. In order to comprehend the enormous amount of data that results from multiparametric methods, including MR, histology, proteomics etc., the need for methods that deal with the high amount of information is increased. Such methods exist, *e.g.* the feature selection method presented, but they need to be further optimized to the data provided by the multiple methods discussed above.

Before the results from the works of this thesis can be translated to the human situation, several aspects must be considered. For example, apart from the biological differences, how are the associations between MR parameters and tumour tissue affected by the lower magnetic field strength in human MR systems? Are the contrast tracer kinetics comparable between a subcutaneously grown tumour on a mouse and a tumour in a patient considering, *e.g.*, the differences in heart rate, tracer transport distances, tumour size, TME and vessel configuration and function?

The exposure situation of radionuclide therapy, with prolonged irradiation, relatively low dose-rate and differences in radiation quality is very different compared with external radiotherapy. Differences in effects on MR parameters should be studied in order to investigate if findings from one irradiation type can be generalized to other types, and effects from other types of treatments, such as chemotherapy, should also be evaluated. Furthermore, tumour types other than the NET studied in this project may present differences in biological characteristics, such as vascularization, and they may respond differently to treatment, *e.g.* by different cell death modalities. It is therefore necessary to expand studies to include other tumour types as well, before general conclusions on MR based tumour tissue characterization and response assessment can be made.

Acknowledgements

They say that behind every successful man there is a woman – I had three!

This work would not have been possible without my main supervisor **Eva Forssell-Aronsson**. Thank you, Eva, for your support, for the fun and always encouraging meetings and retreats with lots of laughs, and for your advises on science and scientific writing. I will miss Hindås! Perhaps most important for the final success of the project, thank you for the support and encouragement each time, and there were a few, seemingly insurmountable problems occurred, such as the shut-down of the MR facility, cancer resistant animals or world crisis on helium supply, to mention a few. I am also fully aware and thankful for your efforts "behind the scene", in order to extend my employment when I kept running out of time due to the abovementioned problems.

Then there is the endless support provided by my co-supervisor, **Maria Ljungberg**. I would not have finished this work if it wasn't for you Maria! You were the solid foundation that kept me standing whenever I doubted that I would ever reach the finish line, you have listened to me complain when I have felt despair or anger, inspired me to keep learning, and carefully pushed me in the right direction when my own compass, probably too close to all magnets, misguided me, but you definitely failed to teach me how to write short sentences with few commas. I really hope there will be many more prosperous scientific or just friendly meetings over a cup of coffee also in the future. And there will be! We still have some unfinished business.

The third woman behind me is the one I definitely owe most. She always believed in me, supported me, acted interested audience through endless rehearsals of presentations and, during the last couple of months, almost fed and washed me while I did nothing but work, work and work, vacations and weekends. Thank you **Mia**, my fiancée and partner in life, men tack också **Vilma** och **Valter**! Nu ska pappa sluta sitta i källaren och jobba hela tiden. Jag älskar er alla!

I also thank my co-author Prof. **Ola Nilsson** for valuable inputs, analyses and the hours spent at the "Älgen" microscope, teaching me about histology and inspiring me to learn more about biology. Thank you also **Gülay Altiparmak**! Without your hocus-pocus staining procedures, the world, and my thesis, would be less colorful.

What fun would it be if there were no fellow PhD students? Who would you go to conferences with, have too many beers with and, once in a while, have scientific discussions on a similar (secretly low) level with? I have seen them

come and go, but I actually managed to beat **Johan Spetz** to the finish line (although I had a significant head start, $p<0.05$), and for that I am deeply grateful. Johan, together we managed to extend the necessary word count in materials and methods with a few pages, but maybe we learned how to set up future experiment, which I hope we will do together! Thank you also **Oscar Gustafsson**! I don't know how you do it, but you see things I don't see in my own figures and numbers, and it is always fun to discuss them with you, although it may be "lite klurigt" from time to time. Other contemporaries who all made it worthwhile are **Anders, Johanna, Esmaeil, Maria, Niklas, Fia, Anna, Angelica, Sara, Tom, Jonas, Nils, Emil, Britta, Alexa, Jonny, Christina, Emman, Viktor, Ingun** and shooting stars **Malin, Sofia, Arman, Rimon, Linn, Jens, Charlotte, Mikael** and everyone else that I just can't remember at the (very late) moment. Thank you all!

I had the pleasure to spend these years at the highly interesting, educating and always supporting MR centre, where **Maria**, **Oscar**, **Christian K Gustafsson, Maja Sohlin, Åsa Carlsson, Frida Svensson, Maria Hultenmo, Barbro Vikhoff Baaz, Yosef Al-Abasse, Kerstin Lagerstrand, Göran Starck, Jonathan Arvidsson, Christian Waldenberg and Linnéa Andersson** made my time so much easier and fun! **Christian K Gustafsson**, I wish you all the luck with your new endeavours, and hope we will work together again sometime, and thank you for letting me beat you in arm wrestling so easily. Thank you also "down-stairs", for all the help with the DOTS, which we now know were completely unnecessary.

I also owe a great thanks to the department of Radiofysik and MFT, with **Mia, Jeanette, Gunilla** and all others who make life easier and funnier. **Lilian Karlsson** and **Ann Wikström**, you taught me so much about animal handling and lab work that can't be found in books and it is always a pleasure to be in the lab with you guys! I already miss working with you!

Thank you also "7T-gruppen", where **Mikael Hellström**, **Stephan Maier, Sven Ekholm, Göran, Eva, Maria** and others made it possible to proceed with my research by keeping the camera up and running. This is a good opportunity to thank also **Michael Horn**, who introduced me to the 7T system in the beginning of time, as well as the former CPI staff who made me less lonely on the mountain.

Last but not least, thank you family and friends, especially mamma **Monica** and pappa **Tomas** with families, and all my sisters and brothers, also with families. Thank you for accepting and supporting my decision to put so much time and effort in myself! I look forward to being more present from now on. Love you all!

This study was supported by grants from the Swedish Research Council, the Swedish Cancer Society, BioCARE – a National Strategic Research Program at the University of Gothenburg, the King Gustav V Jubilee Clinic Cancer Research Foundation, the Sahlgrenska University Hospital Research Funds, the Assar Gabrielsson Cancer Research Foundation, the Adlerbertska Research Fund, the Wilhelm and Martina Lundgren science trust fund and the Royal Society of Arts and Sciences in Gothenburg (KVVS). We are also grateful to the Proteomics Core Facility at Sahlgrenska Academy, Gothenburg University, who performed the analysis for protein quantification and Inga-Britt and Arne Lundbergs Research Foundations for the donation of the Orbitrap Fusion Tribrid MS instrument used in this analysis.

References

1. Ferlay, J., Soerjomataram, I., Dikshit, R., Eser, S., Mathers, C., Rebelo, M., *et al.*, *Cancer incidence and mortality worldwide: sources, methods and major patterns in GLOBOCAN 2012.* Int J Cancer, 2015. **136**(5): p. 9.
2. Stewart, B., Wild, C.P., *World Cancer Report 2014.* International Agency for Research on Cancer, WHO, 2014.
3. Hanahan, D. and Weinberg, R.A., *The Hallmarks of Cancer.* Cell, 2000. **100**(1): p. 57-70.
4. Hanahan, D. and Weinberg, Robert A., *Hallmarks of Cancer: The Next Generation.* Cell, 2011. **144**(5): p. 646-674.
5. Weber, C.E. and Kuo, P.C., *The tumor microenvironment.* Surgical Oncology, 2012. **21**(3): p. 172-177.
6. Guppy, M., *The hypoxic core: a possible answer to the cancer paradox.* Biochemical and Biophysical Research Communications, 2002. **299**(4): p. 676-680.
7. Groh, C.M., Hubbard, M.E., Jones, P.F., Loadman, P.M., Periasamy, N., Sleeman, B.D., *et al.*, *Mathematical and computational models of drug transport in tumours.* Journal of The Royal Society Interface, 2014. **11**(94).
8. Boucher, Y. and Jain, R.K., *Microvascular pressure is the principal driving force for interstitial hypertension in solid tumors: implications for vascular collapse.* Cancer Res, 1992. **52**(18): p. 5110-4.
9. Hassid, Y., Furman-Haran, E., Margalit, R., Eilam, R. and Degani, H., *Noninvasive Magnetic Resonance Imaging of Transport and Interstitial Fluid Pressure in Ectopic Human Lung Tumors.* Cancer Research, 2006. **66**(8): p. 4159-4166.
10. Boucher, Y., Baxter, L.T. and Jain, R.K., *Interstitial pressure gradients in tissue-isolated and subcutaneous tumors: implications for therapy.* Cancer Res, 1990. **50**(15): p. 4478-84.
11. Heldin, C.H., Rubin, K., Pietras, K. and Ostman, A., *High interstitial fluid pressure - an obstacle in cancer therapy.* Nat Rev Cancer, 2004. **4**(10): p. 806-13.
12. Rofstad, E.K., Gaustad, J.V., Brurberg, K.G., Mathiesen, B., Galappathi, K. and Simonsen, T.G., *Radiocurability is associated with interstitial fluid pressure in human tumor xenografts.* Neoplasia, 2009. **11**(11): p. 1243-51.
13. Milosevic, M.F., Fyles, A.W. and Hill, R.P., *The relationship between elevated interstitial fluid pressure and blood flow in tumors: a bioengineering analysis.* Int J Radiat Oncol Biol Phys, 1999. **43**(5): p. 1111-23.
14. Wiig, H., Tveit, E., Hultborn, R., Reed, R.K. and Weiss, L., *Interstitial fluid pressure in DMBA-induced rat mammary tumours.* Scand J Clin Lab Invest, 1982. **42**(2): p. 159-64.
15. Yao, J.C., Hassan, M., Phan, A., Dagohoy, C., Leary, C., Mares, J.E., *et al.*, *One hundred years after "carcinoid": epidemiology of and prognostic factors for neuroendocrine tumors in 35,825 cases in the United States.* J Clin Oncol, 2008. **26**(18): p. 3063-72.
16. Zitzmann, K., Rüden, J.v., Brand, S., Göke, B., Lichtl, J., Spöttl, G., *et al.*, *Compensatory activation of Akt in response to mTOR and Raf inhibitors – A rationale for dual-targeted therapy approaches in neuroendocrine tumor disease.* Cancer Letters, 2010. **295**(1): p. 100-109.
17. Strosberg, J., *Neuroendocrine tumours of the small intestine.* Best Practice & Research Clinical Gastroenterology. **26**(6): p. 755-773.
18. Forssell-Aronsson, E., Spetz, J. and Ahlman, H., *Radionuclide therapy via SSTR: future aspects from experimental animal studies.* Neuroendocrinology, 2013. **97**(1): p. 86-98.
19. Pouget, J.P., Lozza, C., Deshayes, E., Boudousq, V. and Navarro-Teulon, I., *Introduction to radiobiology of targeted radionuclide therapy.* Front Med, 2015. **2**(12).
20. Orth, M., Lauber, K., Niyazi, M., Friedl, A.A., Li, M., Maihöfer, C., *et al.*, *Current concepts in clinical radiation oncology.* Radiation and Environmental Biophysics, 2014. **53**(1): p. 1-29.
21. Kwekkeboom, D.J., de Herder, W.W., Kam, B.L., van Eijck, C.H., van Essen, M., Kooij, P.P., *et al.*, *Treatment with the radiolabeled somatostatin analog [177 Lu-DOTA 0,Tyr3]octreotate: toxicity, efficacy, and survival.* J Clin Oncol, 2008. **26**(13): p. 2124-30.

22. Sward, C., Bernhardt, P., Ahlman, H., Wangberg, B., Forssell-Aronsson, E., Larsson, M., *et al.*, *[177Lu-DOTA 0-Tyr 3]-octreotate treatment in patients with disseminated gastroenteropancreatic neuroendocrine tumors: the value of measuring absorbed dose to the kidney.* World J Surg, 2010. **34**(6): p. 1368-72.
23. Dominietto, M. and Rudin, M., *Could magnetic resonance provide in vivo histology?* Front Genet, 2014. **4**(298): p. 13.
24. Marcus, C.D., Ladam-Marcus, V., Cucu, C., Bouché, O., Lucas, L. and Hoeffel, C., *Imaging techniques to evaluate the response to treatment in oncology: Current standards and perspectives.* Critical Reviews in Oncology/Hematology, 2009. **72**(3): p. 217-238.
25. Rudin, M., *Imaging readouts as biomarkers or surrogate parameters for the assessment of therapeutic interventions.* European Radiology, 2007. **17**(10): p. 2441-2457.
26. Fass, L., *Imaging and cancer: A review.* Molecular Oncology, 2008. **2**(2): p. 115-152.
27. Cai, J. and Li, F., *Single-photon emission computed tomography tracers for predicting and monitoring cancer therapy.* Curr Pharm Biotechnol, 2013. **14**(7): p. 693-707.
28. Forssell-Aronsson, E., Kjellen, E., Mattsson, S. and Hellstrom, M., *Medical imaging for improved tumour characterization, delineation and treatment verification.* Acta Oncol, 2002. **41**(7-8): p. 604-14.
29. Stroobants, S., Goeminne, J., Seegers, M., Dimitrijevic, S., Dupont, P., Nuyts, J., *et al.*, *18FDG-Positron emission tomography for the early prediction of response in advanced soft tissue sarcoma treated with imatinib mesylate (Glivec).* Eur J Cancer, 2003. **39**(14): p. 2012-20.
30. Antoch, G., Stattaus, J., Nemat, A.T., Marnitz, S., Beyer, T., Kuehl, H., *et al.*, *Non-small cell lung cancer: dual-modality PET/CT in preoperative staging.* Radiology, 2003. **229**(2): p. 526-33.
31. Kim, H.S., Lee, K.S., Ohno, Y., van Beek, E.J. and Biederer, J., *PET/CT versus MRI for diagnosis, staging, and follow-up of lung cancer.* J Magn Reson Imaging, 2015. **42**(2): p. 247-60.
32. Iima, M. and Bihan, D.L., *Clinical Intravoxel Incoherent Motion and Diffusion MR Imaging: Past, Present, and Future.* Radiology, 2016. **278**(1): p. 13-32.
33. Kurhanewicz, J., Vigneron, D., Carroll, P. and Coakley, F., *Multiparametric magnetic resonance imaging in prostate cancer: present and future*: Curr Opin Urol. 2008 Jan;18(1):71-7. doi:10.1097/MOU.0b013e3282f19d01.
34. Kumar, C., Shetake, N., Desai, S., Kumar, A., Samuel, G. and Pandey, B.N., *Relevance of radiobiological concepts in radionuclide therapy of cancer.* International Journal of Radiation Biology, 2016. **92**(4): p. 173-186.
35. Le Bihan, D., Breton, E., Lallemand, D., Aubin, M.L., Vignaud, J. and Laval-Jeantet, M., *Separation of diffusion and perfusion in intravoxel incoherent motion MR imaging.* Radiology, 1988. **168**(2): p. 497-505.
36. Jensen, J.H. and Helpern, J.A., *MRI quantification of non-Gaussian water diffusion by kurtosis analysis.* Nmr in Biomedicine, 2010. **23**(7): p. 698-710.
37. Neil, J.J. and Bretthorst, G.L., *On the use of bayesian probability theory for analysis of exponential decay date: An example taken from intravoxel incoherent motion experiments.* Magnetic Resonance in Medicine, 1993. **29**(5): p. 642-647.
38. Barbieri, S., Donati, O.F., Froehlich, J.M. and Thoeny, H.C., *Impact of the calculation algorithm on biexponential fitting of diffusion-weighted MRI in upper abdominal organs.* Magnetic Resonance in Medicine, 2015.
39. Orton, M.R., Collins, D.J., Koh, D.M. and Leach, M.O., *Improved intravoxel incoherent motion analysis of diffusion weighted imaging by data driven Bayesian modeling.* Magn Reson Med, 2014. **71**(1): p. 411-20.
40. Barbieri, S., Donati, O.F., Froehlich, J.M. and Thoeny, H.C., *Impact of the calculation algorithm on biexponential fitting of diffusion-weighted MRI in upper abdominal organs.* Magn Reson Med, 2015. **8**(10): p. 25765.
41. Padhani, A.R., Liu, G., Koh, D.M., Chenevert, T.L., Thoeny, H.C., Takahara, T., *et al.*, *Diffusion-weighted magnetic resonance imaging as a cancer biomarker: consensus and recommendations.* Neoplasia, 2009. **11**(2): p. 102-25.

42. Eccles, C.L., Haider, E.A., Haider, M.A., Fung, S., Lockwood, G. and Dawson, L.A., *Change in diffusion weighted MRI during liver cancer radiotherapy: Preliminary observations.* Acta Oncologica, 2009. **48**(7): p. 1034-1043.
43. Hill, D.K., Kim, E., Teruel, J.R., Jamin, Y., Wideroe, M., Sogaard, C.D.*, et al.*, *Diffusion-weighted MRI for early detection and characterization of prostate cancer in the transgenic adenocarcinoma of the mouse prostate model.* J Magn Reson Imaging, 2016. **43**(5): p. 1207-17.
44. Joo, I.L., JM. Han, JK. Choi, BI., *Intravoxel Incoherent Motion Diffusion-weighted MR Imaging for Monitoring the Therapeutic Efficacy of the Vascular Disrupting Agent CKD-516 in Rabbit VX2 Liver Tumors.* Radiology, 2014. **272**(2): p. 417-426.
45. van Rijswijk, C.S., Kunz, P., Hogendoorn, P.C., Taminiau, A.H., Doornbos, J. and Bloem, J.L., *Diffusion-weighted MRI in the characterization of soft-tissue tumors.* Journal of Magnetic Resonance Imaging, 2002. **15**(3): p. 302-307.
46. Kim, S., Decarlo, L., Cho, G.Y., Jensen, J.H., Sodickson, D.K., Moy, L.*, et al.*, *Interstitial fluid pressure correlates with intravoxel incoherent motion imaging metrics in a mouse mammary carcinoma model.* Nmr in Biomedicine, 2012. **25**(5): p. 787-794.
47. Padhani, A.R., Krohn, K.A., Lewis, J.S. and Alber, M., *Imaging oxygenation of human tumours.* European Radiology, 2007. **17**(4): p. 861-872.
48. Egeland, T.A.M., Simonsen, T.G., Gaustad, J.-V., Gulliksrud, K., Ellingsen, C. and Rofstad, E.K., *Dynamic Contrast-Enhanced Magnetic Resonance Imaging of Tumors: Preclinical Validation of Parametric Images.* Radiation Research, 2009. **172**(3): p. 339-347.
49. Punwani, S., *Contrast enhanced MR imaging of female pelvic cancers: Established methods and emerging applications.* European Journal of Radiology, 2011. **78**(1): p. 2-11.
50. Bol, K., Haeck, J.C., Groen, H.C., Niessen, W.J., Bernsen, M.R., de Jong, M.*, et al.*, *Can DCE-MRI Explain the Heterogeneity in Radiopeptide Uptake Imaged by SPECT in a Pancreatic Neuroendocrine Tumor Model?*: PLoS One. 2013;8(10):e77076. doi:10.1371/journal.pone.0077076.
51. Cho, H., Ackerstaff, E., Carlin, S., Lupu, M.E., Wang, Y., Rizwan, A.*, et al.*, *Noninvasive Multimodality Imaging of the Tumor Microenvironment: Registered Dynamic Magnetic Resonance Imaging and Positron Emission Tomography Studies of a Preclinical Tumor Model of Tumor Hypoxia.* Neoplasia (New York, N.Y.), 2009. **11**(3): p. 247-259.
52. Rofstad, E.K., Galappathi, K. and Mathiesen, B.S., *Tumor Interstitial Fluid Pressure—A Link between Tumor Hypoxia, Microvascular Density, and Lymph Node Metastasis.* Neoplasia (New York, N.Y.), 2014. **16**(7): p. 586-594.
53. Hompland, T., Ellingsen, C. and Rofstad, E.K., *Preclinical evaluation of Gd-DTPA and gadomelitol as contrast agents in DCE-MRI of cervical carcinoma interstitial fluid pressure.* BMC Cancer, 2012. **12**: p. 544-544.
54. Gulliksrud, K., Hompland, T., Galappathi, K. and Rofstad, E.K., *Assessment of tumor hypoxia and interstitial fluid pressure by gadomelitol-based dynamic contrast-enhanced magnetic resonance imaging.* Radiotherapy and Oncology, 2011. **101**(1): p. 217-222.
55. Ravoori, M.K., Nishimura, M., Singh, S.P., Lu, C., Han, L., Hobbs, B.P.*, et al.*, *Tumor T1 Relaxation Time for Assessing Response to Bevacizumab Anti-Angiogenic Therapy in a Mouse Ovarian Cancer Model.* PLoS ONE, 2015. **10**(6): p. e0131095.
56. Lescher, S., Jurcoane, A., Veit, A., Bahr, O., Deichmann, R. and Hattingen, E., *Quantitative T1 and T2 mapping in recurrent glioblastomas under bevacizumab: earlier detection of tumor progression compared to conventional MRI.* Neuroradiology, 2015. **57**(1): p. 11-20.
57. Heijmen, L., ter Voert, E.E.G.W., Oyen, W.J.G., Punt, C.J.A., van Spronsen, D.J., Heerschap, A.*, et al.*, *Multimodality Imaging to Predict Response to Systemic Treatment in Patients with Advanced Colorectal Cancer.* PLoS One, 2015. **10**(4): p. e0120823.
58. Kölby, L., Bernhardt, P., Ahlman, H., Wängberg, B., Johanson, V., Wigander, A.*, et al.*, *A transplantable human carcinoid as model for somatostatin receptor-mediated and amine transporter-mediated radionuclide uptake.* The American journal of pathology, 2001. **158**(2): p. 745.

59. Dalmo, J., Spetz, K., Montelius, M., Langen, B., Arvidsson, Y., Johansson, H., *et al.*, *Priming increases the anti-tumor effect and therapeutic window of 177Lu-octreotate in nude mice bearing human small intestine neuroendocrine tumor GOT1.* Revision.
60. Veta, M., van Diest, P.J., Kornegoor, R., Huisman, A., Viergever, M.A. and Pluim, J.P., *Automatic nuclei segmentation in H&E stained breast cancer histopathology images.* PLoS One, 2013. **8**(7): p. e70221.
61. Kroemer, G., Galluzzi, L., Vandenabeele, P., Abrams, J., Alnemri, E.S., Baehrecke, E.H., *et al.*, *Classification of cell death: recommendations of the Nomenclature Committee on Cell Death 2009.* Cell Death Differ, 2008. **16**(1): p. 3-11.
62. Spetz J, M.M., Berger E, Sihlbom C, Ljungberg M, Helou K, Nilsson O, Forssell-Aronsson *Time-dependent proteomic response of GOT1 human small intestine neuroendocrine tumor after 177Lu-octreotate therapy.*
63. Ashburner, M., Ball, C.A., Blake, J.A., Botstein, D., Butler, H., Cherry, J.M., *et al.*, *Gene ontology: tool for the unification of biology. The Gene Ontology Consortium.* Nat Genet, 2000. **25**(1): p. 25-9.
64. Tibshirani, R., *Regression shrinkage and selection via the lasso.* Journal of the Royal Statistical Society. Series B (Methodological), 1996: p. 267-288.
65. Paul, D., Bair, E., Hastie, T. and Tibshirani, R., *" Preconditioning" for feature selection and regression in high-dimensional problems.* The Annals of Statistics, 2008: p. 1595-1618.
66. Eisenhauer, E., Therasse, P., Bogaerts, J., Schwartz, L., Sargent, D., Ford, R., *et al.*, *New response evaluation criteria in solid tumours: revised RECIST guideline (version 1.1).* European Journal of Cancer, 2009. **45**(2): p. 228-247.
67. Mehrara, E., Forssell-Aronsson, E. and Bernhardt, P., *Objective assessment of tumour response to therapy based on tumour growth kinetics.* British journal of cancer, 2011. **105**(5): p. 682-686.
68. Weber, W.A., *Assessing Tumor Response to Therapy.* Journal of Nuclear Medicine, 2009. **50**(Suppl 1): p. 1S-10S.
69. Jensen, M., Jorgensen, J., Binderup, T. and Kjaer, A., *Tumor volume in subcutaneous mouse xenografts measured by microCT is more accurate and reproducible than determined by 18F-FDG-microPET or external caliper.* BMC Medical Imaging, 2008. **8**(1): p. 16.
70. Carlson, S.K., Classic, K.L., Bender, C.E. and Russell, S.J., *Small animal absorbed radiation dose from serial micro-computed tomography imaging.* Mol Imaging Biol, 2007. **9**(2): p. 78-82.
71. Workman, P., Aboagye, E.O., Balkwill, F., Balmain, A., Bruder, G., Chaplin, D.J., *et al.*, *Guidelines for the welfare and use of animals in cancer research.* Br J Cancer, 2010. **102**(11): p. 1555-1577.
72. Tofts, P.S., Brix, G., Buckley, D.L., Evelhoch, J.L., Henderson, E., Knopp, M.V., *et al.*, *Estimating kinetic parameters from dynamic contrast-enhanced t1-weighted MRI of a diffusable tracer: Standardized quantities and symbols.* Journal of Magnetic Resonance Imaging, 1999. **10**(3): p. 223-232.
73. Barnes, S.L., Whisenant, J.G., Loveless, M.E. and Yankeelov, T.E., *Practical Dynamic Contrast Enhanced MRI in Small Animal Models of Cancer: Data Acquisition, Data Analysis, and Interpretation.* Pharmaceutics, 2012. **4**(3): p. 442.
74. Knopp, M., Weiss, E., Sinn, H., Mattern, J., Junkermann, H., Radeleff, J., *et al.*, *Pathophysiologic basis of contrast enhancement in breast tumors.* Journal of Magnetic Resonance Imaging, 1999. **10**(3): p. 260-266.
75. Knopp, M.V., von Tengg-Kobligk, H. and Choyke, P.L., *Functional Magnetic Resonance Imaging in Oncology for Diagnosis and Therapy Monitoring.* Molecular Cancer Therapeutics, 2003. **2**(4): p. 419-426.
76. Haeck, J.C., Bol, K., de Ridder, C.M., Brunel, L., Fehrentz, J.A., Martinez, J., *et al.*, *Imaging heterogeneity of peptide delivery and binding in solid tumors using SPECT imaging and MRI.* EJNMMI Res, 2016. **6**(1): p. 016-0160.
77. Jain, R.K., *Normalizing tumor microenvironment to treat cancer: bench to bedside to biomarkers.* J Clin Oncol, 2013. **31**(17): p. 2205-18.
78. Sorace, A.G., Quarles, C.C., Whisenant, J.G., Hanker, A.B., McIntyre, J.O., Sanchez, V.M., *et al.*, *Trastuzumab improves tumor perfusion and vascular delivery of cytotoxic therapy in a murine*

model of HER2+ breast cancer: preliminary results. Breast Cancer Research and Treatment, 2016. **155**(2): p. 273-284.
79. Parker, G.J.M., Suckling, J., Tanner, S.F., Padhani, A.R., Revell, P.B., Husband, J.E.*, et al.*, *Probing tumor microvascularity by measurement, analysis and display of contrast agent uptake kinetics.* Journal of Magnetic Resonance Imaging, 1997. **7**(3): p. 564-574.
80. Li, L.Z., Zhou, R., Xu, H.N., Moon, L., Zhong, T., Kim, E.J.*, et al.*, *Quantitative magnetic resonance and optical imaging biomarkers of melanoma metastatic potential.* Proceedings of the National Academy of Sciences, 2009. **106**(16): p. 6608-6613.
81. Zahra, M.A., Hollingsworth, K.G., Sala, E., Lomas, D.J. and Tan, L.T., *Dynamic contrast-enhanced MRI as a predictor of tumour response to radiotherapy.* The Lancet Oncology, 2007. **8**(1): p. 63-74.
82. Yamashita, Y., Baba, T., Baba, Y., Nishimura, R., Ikeda, S., Takahashi, M.*, et al.*, *Dynamic Contrast-enhanced MR Imaging of Uterine Cervical Cancer: Pharmacokinetic Analysis with Histopathologic Correlation and Its Importance in Predicting the Outcome of Radiation Therapy.* Radiology, 2000. **216**(3): p. 803-809.
83. Baudelet, C., Cron, G.O., Ansiaux, R., Crokart, N., DeWever, J., Feron, O.*, et al.*, *The role of vessel maturation and vessel functionality in spontaneous fluctuations of T2*-weighted GRE signal within tumors.* NMR Biomed, 2006. **19**(1): p. 69-76.
84. Baudelet, C. and Gallez, B., *How does blood oxygen level-dependent (BOLD) contrast correlate with oxygen partial pressure (pO2) inside tumors?* Magn Reson Med, 2002. **48**(6): p. 980-6.
85. Höckel, M. and Vaupel, P., *Tumor Hypoxia: Definitions and Current Clinical, Biologic, and Molecular Aspects.* Journal of the National Cancer Institute, 2001. **93**(4): p. 266-276.
86. Rodrigues, L.M., Howe, F.A., Griffiths, J.R. and Robinson, S.P., *Tumor R2* is a prognostic indicator of acute radiotherapeutic response in rodent tumors.* Journal of Magnetic Resonance Imaging, 2004. **19**(4): p. 482-488.
87. Li, S.P., Taylor, N.J., Makris, A., Ah-See, M.-L.W., Beresford, M.J., Stirling, J.J.*, et al.*, *Primary Human Breast Adenocarcinoma: Imaging and Histologic Correlates of Intrinsic Susceptibility-weighted MR Imaging before and during Chemotherapy.* Radiology, 2010. **257**(3): p. 643-652.
88. Tseng, J., Dunnwald, L.K., Schubert, E.K., Link, J.M., Minoshima, S., Muzi, M.*, et al.*, *18F-FDG Kinetics in Locally Advanced Breast Cancer: Correlation with Tumor Blood Flow and Changes in Response to Neoadjuvant Chemotherapy.* Journal of Nuclear Medicine, 2004. **45**(11): p. 1829-1837.
89. Li, K.L., Henry, R.G., Wilmes, L.J., Gibbs, J., Zhu, X., Lu, Y.*, et al.*, *Kinetic assessment of breast tumors using high spatial resolution signal enhancement ratio (SER) imaging.* Magn Reson Med, 2007. **58**(3): p. 572-81.
90. Kim, J.Y., Kim, S.H., Kim, Y.J., Kang, B.J., An, Y.Y., Lee, A.W.*, et al.*, *Enhancement parameters on dynamic contrast enhanced breast MRI: do they correlate with prognostic factors and subtypes of breast cancers?* Magnetic Resonance Imaging, 2015. **33**(1): p. 72-80.
91. Koo, H.R., Cho, N., Song, I.C., Kim, H., Chang, J.M., Yi, A.*, et al.*, *Correlation of perfusion parameters on dynamic contrast-enhanced MRI with prognostic factors and subtypes of breast cancers.* Journal of Magnetic Resonance Imaging, 2012. **36**(1): p. 145-151.
92. Partridge, S.C., Vanantwerp, R.K., Doot, R.K., Chai, X., Kurland, B.F., Eby, P.R.*, et al.*, *Association between serial dynamic contrast-enhanced MRI and dynamic 18F-FDG PET measures in patients undergoing neoadjuvant chemotherapy for locally advanced breast cancer.* J Magn Reson Imaging, 2010. **32**(5): p. 1124-31.
93. Eby, P.R., Partridge, S.C., White, S.W., Doot, R.K., Dunnwald, L.K., Schubert, E.K.*, et al.*, *Metabolic and Vascular Features of Dynamic Contrast-enhanced Breast Magnetic Resonance Imaging and 15O-Water Positron Emission Tomography Blood Flow in Breast Cancer.* Academic Radiology, 2008. **15**(10): p. 1246-1254.
94. Kölby, L., Bernhardt, P., Johanson, V., Schmitt, A., Ahlman, H., Forssell-Aronsson, E.*, et al.*, *Successful receptor-mediated radiation therapy of xenografted human midgut carcinoid tumour.* Br J Cancer, 2005. **93**(10): p. 1144-1151.
95. Gulliksrud, K., Brurberg, K.G. and Rofstad, E.K., *Dynamic contrast-enhanced magnetic resonance imaging of tumor interstitial fluid pressure.* Radiotherapy and Oncology, 2009. **91**(1): p. 107-113.

96. Haider, M.A., Sitartchouk, I., Roberts, T.P., Fyles, A., Hashmi, A.T. and Milosevic, M., *Correlations between dynamic contrast-enhanced magnetic resonance imaging–derived measures of tumor microvasculature and interstitial fluid pressure in patients with cervical cancer.* Journal of Magnetic Resonance Imaging, 2007. **25**(1): p. 153-159.
97. Baxter, L.T. and Jain, R.K., *Transport of fluid and macromolecules in tumors. I. Role of interstitial pressure and convection.* Microvascular Research, 1989. **37**(1): p. 77-104.
98. Meyn, R.E., *Apoptosis and response to radiation: implications for radiation therapy.* Oncology (Williston Park, NY), 1997. **11**(3): p. 349-56; discussion 356, 361, 365.
99. Figueiras, R.G., Padhani, A.R., Goh, V.J., Vilanova, J.C., Gonzalez, S.B., Martin, C.V*., et al.*, *Novel oncologic drugs: what they do and how they affect images.* Radiographics, 2011. **31**(7): p. 2059-91.
100. Gambarota, G., Hitti, E., Leporq, B., Saint-Jalmes, H. and Beuf, O., *Eliminating the blood-flow confounding effect in intravoxel incoherent motion (IVIM) using the non-negative least square analysis in liver.* Magn Reson Med, 2016. **5**(10): p. 26085.